Raman and Photoluminescence Studies of In-plane Anisotropic Layered Materials

by

Anupum Pant

A Dissertation Presented in Partial Fulfillment
of the Requirements for the Degree
Master of Science

Approved April 2016 by the
Graduate Supervisory Committee:

Sefaattin Tongay, Chair
Terry L. Alford
Ximin He

ARIZONA STATE UNIVERSITY

May 2016

ABSTRACT

This thesis presents systematic studies on angle dependent Raman and Photoluminescence (PL) of a new class of layered materials, Transition Metal Trichalcogenides (TMTCs), which are made up of layers possessing anisotropic structure within the van-der-Waals plane. The crystal structure of individual layer of MX_3 compounds consists of aligned nanowire like 1D chains running along the b-axis direction. The work focuses on the growth of two members of this family - ZrS_3 and TiS_3 - through Chemical Vapor Transport Method (CVT), with consequent angle dependent Raman and PL studies which highlight their in-plane optically anisotropic properties. Results highlight that the optical properties of few-layer flakes are highly anisotropic as evidenced by large PL intensity variation with polarization direction (in ZrS_3) and an intense variation in Raman intensity with variation in polarization direction (in both ZrS_3 and TiS_3).

Results suggest that light is efficiently absorbed when E-field of the polarized incident excitation laser is polarized along the chain (b-axis). It is greatly attenuated and absorption is reduced when field is polarized perpendicular to the length of 1D-like chains, as wavelength of the exciting light is much longer than the width of each 1D chain. Observed PL variation with respect to the azimuthal flake angle is similar to what has been previously observed in 1D materials like nanowires. However, in TMTCs, since the 1D chains interact with each other, it gives rise to a unique linear dichroism response that falls between 2D and 1D like behavior. These results not only mark the very first demonstration of high PL polarization anisotropy in 2D systems, but also provide a novel insight into how interaction between adjacent 1D-like chains and the 2D nature of each layer influences the overall optical anisotropy of Quasi-1D materials. The presented results are anticipated to have impact in

technologies involving polarized detection, near-field imaging, communication systems, and bio-applications relying on the generation and detection of polarized light.

DEDICATION

I dedicate this work to my mother, father and brother, for without their early guidance, constant support and unconditional efforts, nothing I did would have been done by me.

ACKNOWLEDGMENTS

Firstly, I would like to express my sincere gratitude to my advisor Prof. Sefaattin Tongay for the continuous support of my Masters study and research, for his patience, motivation, enthusiasm, and immense knowledge. His guidance helped me throughout my research and while putting this thesis together. I could not have imagined having a more supportive advisor and mentor for my Masters study.

Besides my advisor, I would like to thank the rest of my thesis committee: Prof. Terry Alford and Prof. Ximin He, for their encouragement, insightful comments, and interesting questions.

My sincere thanks also goes to Dr. Hasan Sahin and Dr. Engin Torun from University of Antwerp, for corroborating my experimental data with timely and meticulous theoretical calculations. I would also like to thank Dr. Emmanuel Soignard in contributing by helping with XRD measurements and interpreting Raman data, and Mr. David Wright for assisting in sealing tubes for bulk crystal growth, as crystal growth of TiS_3 and ZrS_3 would not have been possible without him.

I thank my lab fellows in Dr. Tongay Group at Arizona State University: Dr. Aslihan Tuna, Kedi Wu, Hui Cai, Bin Chen, Sijie Yang, Xi Fan and Wilson Kong, some of whom who were experienced in the lab made it smooth for me to transition into the laboratory, for their direct and indirect contributions to this project, for the sleepless nights we were working together before deadlines, and for all the fun we have had in the last two years.

Last but not the least, I would like to thank my family, my parents Vinod Kumar Pant and Aruna Pant, and brother Sukumar Pant for supporting me in every way throughout my life and providing me with a metaphorical pedestal that made it possible for me to rise.

TABLE OF CONTENTS

CHAPTER Page

CHAPTER Page

LIST OF FIGURES

Figure Page

Chapter 1

INTRODUCTION

1.1 Two-Dimensional Layered Materials (2DLMs)

Layered materials, as the name suggests are crystalline materials consisting of weakly coupled layers of two dimensional (2D) sheets of single unit cell thicknesses, also colloquially known as 2D materials [1]. This fairly young branch of materials science encompassing 2D materials, experienced a burst of scientific interest when, in the year 2005, Andre K. Geim and Konstantin S. Novoselov University of Manchester, UK, first isolated and studied the remarkable properties of 2D Graphite - Graphene - a single atomic layer of consisting of a hexagonal mesh of carbon atoms [2]. This ground breaking discovery of a free-standing, atmospherically stable 2D material with outstanding properties also won them 2010 Nobel Prize in Physics. Since then, the scientific interest in Graphene [3] and other 2D materials has been continuously growing at a rapid pace. A citation report generated using a feature of thomson reuters web of science, for the search term "2D materials" has been shown for reference in figure 1.

The very fact that 2D materials consist of layers of 2D sheets coupled via the van-der-Waals interaction makes them so interesting. Since this inter-layer interaction is much weaker than the forces which hold the atoms in a single layer together, it is far to easy to separate 2D sheets of atoms from a bulk crystal using simple techniques like mechanical cleavage [1]. When a 2D layer of a material stands freely, or on a miscellaneous substrate, not interacting with the bulk part of the crystal, the material

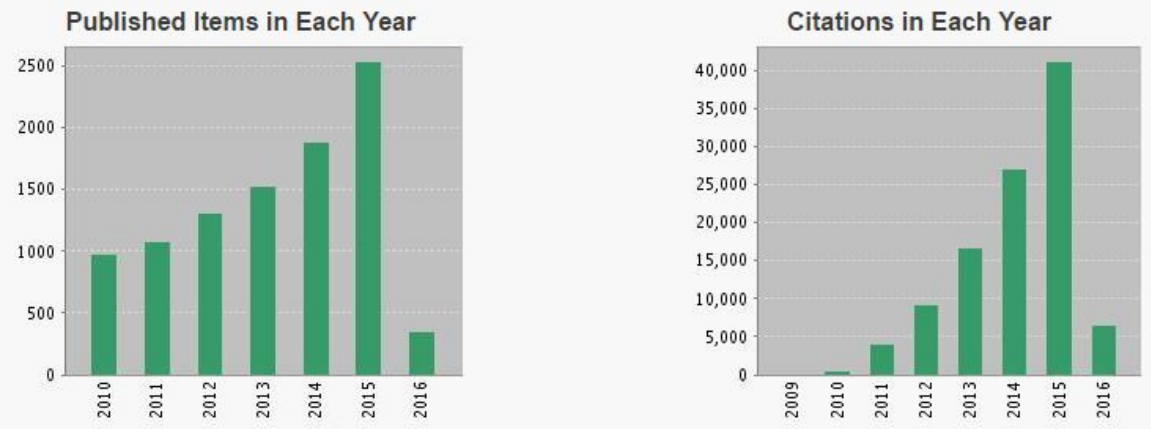

Figure 1. A citation report generated for the search term "2D materials" - from 2010 to present, showing the growing scientific interest in 2D materials.

exhibits physical properties which are significantly different from the same material in bulk form. In fact, these vastly different properties often are observed to be on the more desirable side [4].

The layers in 2D materials, like individual entities, have chemically passivated surfaces. This allows their stacking of one layer on another to form van-der-Waals heterojuntions (a junction consisting of two different layered materials) or a homojunction (stack consisting layers of the same material) without forming a chemical bond at the interface [5, 6]. This allows formation of atomically sharp junctions [7] of materials with minimum band edge smearing. Besides, 2D materials have also been shown to form lateral junctions with atomically sharp interfaces through direct Chemical Vapor Deposition (CVD) synthesis. Owing to these merits, and the fact that these are the thinnest semiconductors, consisting of just the junction and 2D materials enable us to fabricate novel devices with unforeseen properties. The interface which dominated the overall device characteristics has itself become the device with the advent of 2D materials.

Presently, a huge number of theoretical and experimental materials populate the library of known 2D materials. Out of these, Graphene, hexagonal Boron Nitride (h-BN) and Transition metal dichalcogenides (TMDCs) such as MoS_2 are the most popular and well explored materials. These have briefly been introduced in the following sections.

1.1.1 Graphene and Hexagonal Boron Nitride

As briefly touched in the previous section, Graphene is one of the several known allotropes of carbon which consists of a atomically thin sheet of hexagonal mesh of sp^2 hybridized carbon atoms. Although it has been under investigation for more than 60 years now, Graphene was experimentally first isolated only recently [2]. Graphene, like other layered materials can be synthesized by top-down methods such as exfoliation, or can be grown using bottom-up methods such as CVD [8].

AFM nano-indentation tests show an ultimate tensile strength of 130 GPa [9], which makes Graphene the strongest material ever measured. Besides being strong, Graphene is also extremely light. It is estimated that a single square meter of pristine Graphene would measure 0.77 mg and would still be strong enough to support 4 kg. Besides, it has the exceptional elastic properties (elastic modulus in the order of 1 TPa) [9] which allow it to retain its original form after great amounts of strain.

Most of what makes Graphene as a potential game changer in the short run are its electronic properties. Graphene is a gap-less semiconductor. Near the six corners of Graphene's Brillouin zone, known as Dirac points where the cone shaped band edges touch, both the conduction and valence band edges have a linear dispersion [2]. The points at which the cones touch are called the Dirac points, and in a neutral Graphene

the fermi level crosses this point. The linear dispersion also results in carriers to behave as massless Dirac Fermions, and enables carriers to move at the speed of light, enabling high mobility values [2]. High mobility ($>10^5$ $cm^2V^{-1}s^{-1}$), field-effect sensitivity and the ease of placing contacts has made Graphene an attractive candidate for devices such as field effect transistors [10]. Besides that scalability in the deposition has been demonstrated to up-to 30 inch sheets through roll-to-roll printing [11]. This, and other properties like its atmospheric stability, chemical stability, ability to bend it, and the fact that it absorbs a very small fraction of light (2.3%) [12] makes it a potential candidate for transparent conductors in commercial applications such as solar cells coatings [13] and liquid crystal displays (LCDs) [14] etc.

Hexagonal Boron Nitride (h-BN), aslo known as white graphene is another highly explored layered material with a network of regular Boron-Nitrogen hexagons [15]. It is a wide band gap semiconductor with a band gap in the ranges of deep UV (5.0 to 6.0 eV) [16, 17]. Without the presence of dangling bonds on the surface, it is chemically & thermally stable and serves as a great dielectric substrate, or encapsulating material, for other 2DLM based devices [18]. Synthesis methods such as mechanical exfoliation [19], chemical exfoliation [20], large area CVD [15] etc. for h-BN have been widely explored too.

Despite the extensive scientific advancement in the field of Graphene, several issues still need to be addressed. For one, the actual mobility of deposited Graphene sheets is far lower than the high theoretical mobility of Graphene [21]. Based on the substrate or the depositing procedure, the mobility achieved is still highly limited [22]. More importantly, the very fact that Graphene is a zero band gap semiconductor makes it impossible to achieve high on-off ratios in the field effect devices [10]. Although a number of techniques to introduce a band gap such as strain [23, 24], substrate

interaction [25] and breaking inversion symmetry [26, 27], have been proposed, they all come with their own set of problems and a robust technique for opening a band gap in Graphene still remains elusive.

1.1.2 Transition Metal Dichalcogenides (TMDCs)

Transition Metal Dichalcogenides, or compounds commonly known as TMDCs (or TMDs) are a large group of materials with a common chemical representation - MX_2. Here, M represents a transition metal from group IV (Ti, Zr or Hf), group V (V, Nb or Ta) or group VI (Mo, W), and X represents a Chalcogen atom (S, Se or Te) [8]. These materials, like Graphene have layered crystal structures too. However, an intrinsic band gap in a lot of such compounds makes them address one of the major issues associated with Graphene, and makes them stand out.

Depending on the constituent elements of TMDC, the electronic band structure varies greatly. A few are metals, while other can act as semiconductors. and a good number of them exhibit band gaps in infrared and visible ranges, from approximately 0.2 eV to 2.0 eV[28]. Also, other interesting properties associated with TMDCs like MoS_2, where it transitions from indirect to direct band gap when taken from bulk to monolayer sheets, makes them important [4]. Besides that, recent experiments have shown that their electronic structures can be tuned through doping [29], alloying [30], applying strain [31], and by a number of other methods [6].

Unlike the present classes of semiconductors, TMDCs have been shown to exhibit special properties. For instance, the existence of inequivalent valleys leads to a band structure where due to the presence of a new degree of freedom, carriers can exhibit features like valley hall-effect and polarized PL in TMDC monolayers. Based on the

control over the valley degree of freedom, this new space in physics has come to be known as "valleytronics." [32]

In recent times, TMDC monolayers in combination with a variety of other materials and substrates have been used to fabricate a large variety of proof-of-concept devices including, and not limited to, atomically thin FETs with a high on off ratio at room temperature [33, 34], tunable photovoltaic devices [35], photodetectors [36], solar cells [37], sensors [38], Light emitting diodes [35] etc.

1.1.3 Beyond Graphene and TMDCs

Besides Graphene, h-BN and TMDC materials, a whole range of other 2DLM materials have been shown to exist experimentally and theoretically [39, 40]. Ranging from metallic, semiconducting, super conducting and topologically insulating natures, 2D layered materials appear promising to fulfil every possible need for electronics of the future. For instance, Silicon, Boron, Phosphorus, Germanium and Tin based elemental layered analogues of Graphene have been called Silicene [41], Borophene [42], Phosphorene [43], Germanene [44] and Stanene [45]. New materials have come with their own problems, such as stability in air. Phosphorene for instance, is not stable in atmosphere and the first transistor made out of silicene worked for only a few minutes [46]. For the further potential in future commercial applications for such new 2D materials researchers are consistently working towards finding solutions to the problems.

Besides elemental 2D materials, there are other compound based layered materials such as Post-transition metal dichalcogenides (PTMCs - PX) [47, 48, 49], Post-transition metal Iodides (PTMIs - PX_2) [50], Transition metal trichalcogenides

(TMTCs - MX_3)[8] etc. Other little known classes are either under very preliminary examination or are still being unveiled. Either way, the range of properties available with the existing classes of 2DLMs being investigated, present a bright future for the future of electronics.

However, although Graphene, TMDCs and other greatly explored 2DLM materials exhibit a variety of tunable properties with a number of other merits, they posses a rather uniform crystalline structure within the plane. This leads to their uniform isotropic properties within the plane. Hence, along both in-plane crystalline directions, the a-axis and b-axis, they have uniform optical and electronic properties. This limits their usage in devices such as polarized photodetectors and waveguide polarizers.

1.2 Anisotropic Layered Materials

A sub-class of 2DLMs exist which addresses the area where traditional layered materials lack in properties, by exhibiting a strong in-plane anisotropy. A few known materials such as black phosphorus (phosphorene in monolayer form) [51], group-V TMDCs such as ReS_2 & $ReSe_2$ [52], and transition metal trichalcogenides of the form MX_3 have been previously shown to exhibit anisotropic crystal structure and anisotropic properties within the plane [53]. As these materials are structurally anisotropic, angle dependent measurements such as angle dependent Raman, electronic mobility and PL have been previously used to gauge the extent and nature of anisotropy. In particular, high carrier mobility, absorption and structural stability have been found to be higher in one in-plane direction than in the other [51].

1.2.1 Rhenium Sulfide and Rhenium Selenide

ReS_2 and $ReSe_2$ belong to the TMDC group of layered materials of the form MX_2. In this particular case however the transition metal is a group V metal. Although they belong to the same class of materials with the same chemical representation, they behave very differently than TMDCs. These compounds, like TMDCs crystallize with strong covalent bonds in the plane and individual planes (layers) are held together by van-der-Waals forces. The direct optical band gap for ReS_2 has been measured to be 1.26 eV in the bulk and 1.32 eV in monolayer [54]. Measured optical bandgap of ReS_2 on the other hand has been reported to be 1.5-1.6 eV for the bulk and slightly higher for the monolayer [55].

Unlike TMDCs, they crystallize in a distorted $CdCl_2$ structure, with triclinic symmetry. Within the plane, differences in the covalent bonding strength in different directions causes them to exhibit an anisotropic response for linearly polarized light which is incident perpendicular to the basal plane (001). This polarization anisotropy has long been recorded on bulk ReS_2 and $ReSe_2$ crystals [52]. Unlike optically uniaxial TMDC materials these have been known to exhibit biaxial optical properties [56]. Similar anisotropic electronic properties within the van-der-Waals plane were also known [57].

Since the a and b axes are at an angle of 120 or 60 degrees, flakes as seen from the c-axis direction (exfoliated layers) appear as diamond shapes with the same angles, cleaved along the axes [58]. Recently, investigation of ReS_2 using angle dependent Raman spectroscopy revealed that there is an intense variation of recorded Raman intensity with a polarized incident laser when the azimuthal angle of the van-der-Waals plane was varied [59, 60]. This serves as a convenient way to determine the crystalline

direction using Raman measurements. Angle resolved transport measurements have shown a mobility ratio (μ_{max}/μ_{min}) of 3.1 in a six layered device fabricated with twelve electrodes deposited at every 30^o [58].

Overall, ReS_2 and $ReSe_2$ clearly present a class of in-plane anisotropic materials with tunable in-plane transport and optical properties with azimuthal angle [61]. They open up new opportunities for novel nanoelectronic devices where in which anisotropic properties are required.

However, the anisotropic properties observed are either mild, or seem to disappear in thicker flakes (greater than 1-5 layers). Due to practical balance of amount of material available for decent electronic and optical signal, ease of fabrication and preservation of material flexibility, slightly thicker flakes (quasi-2D) seem like a practical direction for layered materials to go in the future. Hence, it is important that the intense polarization dependent properties remain strong at these thicknesses for material application in practical devices.

1.2.2 Black Phosphorus and Phosphorene

Black phosphorus is the most stable isotope of Phosphorus and it exists in layered form. It can be exfoliated into ultra-thin or monolayer forms using micro-mechanical exfoliation. In the monolayer form, it is known as Phosphorene and is not very stable in the air. The monolayer appears in a corrugated structure along one direction and is not technically planar. In the bulk, black phosphorus has a band gap of 0.3 eV and changes significantly depending on the thickness, reaches 1.5 eV in the monolayer form [62, 63]. It has high intrinsic mobilty as well as a suffciently large bandgap to place itself in the list of emerging materials for quality nanoelectronic devices.

Owing to the structural anisotropy (corrugated structure in one direction), black phosphorus shows corresponding anisotropic electronic and optical properties. For ultra-thin layers of black-phosphorus of 15 nm thickness, the measured hall mobility for holes in x and y direction is 1,000 and 600 $cm^2V^{-1}s^{-1}$, respectively. This suggests that holes are lighter in the x direction than in the y direction within the van-der-Waals plane [64]. Also, the optical conductivity was found to be significantly higher in the x direction [64]. Absorption data shows a strong dichroism in layers of black phosphorus depending on the incident laser polarization direction is parallel or perpendicular to the x axis [63]. It is proposed as a convenient method to determine the crystalline orientation using optical methods. Also, ab-initio studies have suggested that the anisotropic mobility in black phosphorus can be tuned using strain [65].

Thus black phosphorus is another good addition to this sub class of 2DLMs which show in-plane anisotropy for applications in the infrared region and in the circumstances where anisotropy in optical and electronic properties are desired. However, the biggest issue associated with single layer black phosphorus is its atmospheric instability, which prevents fabrication of atomically thin devices using Phosphorene. Although it can be dealt with to some extent by using h-BN encapsulation, it still is a seriously challenging issue for the fabrication of robust devices.

1.2.3 Transition Metal Trichalcogenides (TMTCs)

Transition Metal Trichalcogenides (or TMTCs) are the compounds of the form MX_3 where M is a IVB or VB group element and X represents S, Se or Te. They crystallize isomorphically into monoclinic structures with interesting chain like features in the b-axis directions.

They resemble other 2DLMs in a way that they crystallize in layered forms where the individual layers are held together with the help of relatively strong covalent bonds, while the layers are stacked and coupled via weaker van-der-Waals interaction, which allows the isolation of ultrathin or monolayers with the help of simple micro mechanical exfoliation. However, unlike the traditional 2DLMs, MX_3s also fall in the category of anisotropic layered materials as the covalent bonds within the layer vary in their strengths in the different directions (a and b axes). The covalent bonds in the b direction are significantly stronger than the covalent bonds in the a direction.

In the b direction these compounds form chain like structures consisting of MX_6 units as the chain unit cells. The metal in these MX_6 units sit in the center of a trigonal prism and the six corners of the prism are occupied by the chalcogen atoms. The chains are formed with these units sharing their triangular faces. In the direction of these chains, the covalent bonds between the metal and the chalcogen are much stronger than the bonds that connect two chains. This allows the breaking of bonds in a direction much easier and the crystals cleave into elongated rectangles with a significantly high aspect ratio of b to a axis lengths. Also, when grown using vapor techniques, the crystals seem to grow more easily in the b-axis direction than in the a direction. This leads to formation of whisker like crystals. Thus, the name - Quasi one dimensional crystals.

Bulk MX_3 compounds have long been predicted and experimentally shown to exhibit anisotropic optical and electronic properties, owing to their anisotropic crystal structure. The first reports of polarization dependent Raman spectra representing strongly varying intensities of Raman spectra in E||b or E$\perp$b directions can be traced back to the 70s [66]. Polarized optical absorption in the past have also shown a slight variation in the absorption energy and an intense variation in the absorption

depending on the excitation direction [67]. Various other optical measurements on bulk crystals have shown a strong absorption when excited using a polarized laser with polarization along the b-axis direction [68].

However, in the light of present advancements in the directions of layered material, these properties of MX_3 in thin crystal regimes beckon a rekindled interest in quasi-1D materials. Neither a systematic angle dependent study that captures the functional variation of the optical properties with the azimuthal angle have been done previously. To fill this gap, this thesis presents a systematic angle-dependent optical study of the TMTCs (TiS_3 and ZrS_3) as a family of atmospherically stable layered materials with anisotropic transport and optical properties. As they hold a promising potential for nanoelectronic devices where anisotropy is a desirable trait, this work hopes to open avenues for researchers in this area.

Chapter 2

REVIEW OF EXPERIMENTAL METHODS

This chapter briefly describes the major techniques that were used for the preparation and investigation of samples for this thesis. Basic outlines in conjunction with the basic functionality of the setups and modifications used are presented as follows.

2.1 Growth and Sample Preparation

2.1.1 Chemical Vapor Transport (CVT)

Chemical Vapor Transport (CVT) has long been established as a standard synthesis method in laboratories for the production of highly crystalline and pure crystals from their constituent elements. High purity, macro sized single crystals of TMDCs [69] and TMTCs [70] have been grown using these techniques by sealing high purity constituent transition metal (M) and chalcogen (X) in stoichiometric ratio inside an evacuated quartz tube, with or without a transport agent such as iodine (I).

The ampule with the sealed materials and transport agent is then loaded into two zone furnace which has a thermal gradient drop from the place where starting materials are placed, up to the place the crystal is intended to grow. The starting materials (M and X), for instance are placed at a temperature T and are transported using the thermal gradient drop of T-ΔT at the other end of the tube, as shown in figure 2. In a typical endothermic reaction,starting materials are placed in the hotter zone, they turn into vapor and get transported towards the relatively cooler

Figure 2. A schematic of the CVT process in a two zone furnace.

end via the transport agent. For exothermic reactions a reverse set up with transport of precursors from cold to hot end is required. At the other end in the quartz tube, these vapors react and form crystals of the thermodynamically stable compound.

Crystals formed through this technique are usually high in purity, owing to the clean evacuated growth chamber and high purity of the precursor elements. Also, large millimeter to centimeter sized single crystals are often obtained. However the growth rate is rather slow and it may take several days of furnace run to obtain a good yield and large crystals of the desired crystalline compound.

2.1.1.1 Safety

The sealed ampule placed in a furnace with rapid increase in temperature could lead to a lot of heat and pressure to be released inside it. This may lead to an explosion, serious enough to destroy the furnace and cause harm to people around the apparatus. It is of prime importance that the safety concerns associated with this techniques are understood before planning experiments.

One important precaution to take for avoiding such accidents is to ramp the temperature of the furnace at very slow rates (of the order of 0 – reaction temperature in 24 hours). Secondly, great care must be taken while sealing the ampule, so as to not leave condensed oxygen on the surface of the ampule. Thirdly, the ampule should be checked carefully for the presence of any micro-cracks. And finally, care should be taken to seal in precursors totaling not more than a few grams (3 g). It is advised to get the sealing done by a professional who has had extensive previous experience with these kind of experiments.

2.1.2 Sample Preparation

Post CVT, the crystals were carefully stored in polycarbonate sample boxes under vacuum for several days. Further, for the micro Raman and PL measurements the crystals were exfoliated using scotch tape method on to silicon substrates with thermally evaporated layer 290 nm of SiO_2, for legible contrast of ultra-thin layers under optical microscope. For Raman measurements of ZrS_3, to eliminate the 520 cm^{-1} peak from the Silicon, which interfered with a peak of the material, sapphire substrate was used to exfoliate it. For XRD measurements, as grown crystals were simply aligned on the zero background holder such that the x-ray beam spot observes minimum overfilling.

2.1.2.1 Mechanical Exfoliation

To separate layers of single unit lattice thicknesses, or several layer thicknesses, the scotch tape method or the mechanical exfoliation technique has become one of

the most popular techniques as it is a straightforward technique with relatively high scientific yield. In fact, the first ever Graphene monolayer isolated from a flake of graphite was done using this method by Andre Geim and Konstantin Novoselov of University of Manchester, UK. It won them a Nobel Prize in Physics for advances which could not have been possible without this technique [2]. Even after about a decade since it was first used, it is still being widely used in laboratories to extract monolayers from layered materials for studying the significantly different fundamental properties of materials in their thinnest possible forms.

Since angle dependent raman and PL measurements requires a flat flake (for perpendicular laser incidence) which has an area big enough to accomodate the full laser beam spot (greater than 1 μm^2) and a flake which is stable, as in adhering to a substrate, mechanical exfoliation was the ideal sample preparation. Also, ultra-thin or monolayers were not desirable in our design of experiments. Hence for separating flat thin and stable layers of freshly cleaved ZrS_3 and TiS_3, the crystals was not cleaved several times.

First, $1cm^2$ pieces of substrate, sapphire and SiO_2/Si were prepared by scribing the larger wafer with a diamond scribe pen. For exfoliation, a small piece of crystal was first placed on the sticky side of a scotch tape, such that the flat side of the crystal was adhered to the tape. The piece of tape was then folded, and a part of the crystal was then transferred to another piece of tape by sticking together the sticky sides of the tapes. The process was repeated until the crystals appeared dull. The sticky side of the tape with dull crystal pieces on it was put on to one of the $1cm^2$ substrates. An even pressure was applied on top of the tape and it was very slowly peeled off from the substrate.

Under the optical microscope, flat micro sized yellow to orange colored (thick)

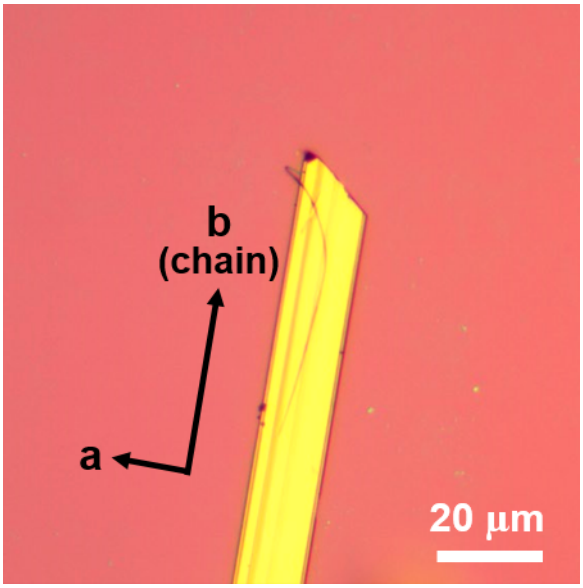

Figure 3. Image of a quasi-1D layered material exfoliated onto SiO_2/Si substrate.

flakes as seen in figure 3 of crystal were observed. These flat surfaces larger than 1 μm^2 were exposed to the laser beam spot to carry out optical studies mentioned as follows.

2.2 Sample Characterization

2.2.1 Raman Spectroscopy

Raman spectroscopy is an efficient, non-contact, nondestructive and a widely used technique for the fingerprinting layered materials without having to conduct any kind (or minimal) sample preparation. Besides, for a well-documented material such as Graphene, Raman spectrum and spatial Raman mapping obtained from this technique can be used to extract out a range of other information like internal stresses, impurities, thermal conductivity, crystalline quality, crystal domain size etc.

2.2.1.1 Raman Scattering

When electromagnetic radiation incidents upon a material, it can undergo either Rayleigh (elastic) scattering, or Raman scattering (inelastic). Raman scattering is however a very low probability event, which is quantitatively about 9 orders of magnitude lesser than Rayleigh scattering. Thus sensitive and accurate equipment is required for its efficient collection.

In the case of Raman scattering, the scattered light can either decrease (stokes) or increase (anti-stokes) in energy, as compared to the incident energy. This energy change is measured in frequency change (Raman shift) and a convenient unit of inverse centimeter (cm^{-1}) is used. We use grating, Rayleigh filter and a CCD detector to collect the intensity of Raman scattered light reflected from the sample. The following figure shows a schematic of our Raman setup.

The spectra is graphically depicted in our measurements as Raman spectra. In this spectra, the intensity of the scattered light (y-axis) is plotted for each energy (frequency) of light (x-axis).

2.2.1.2 Standard Information From Raman

In the big picture, Raman spectrum consists a number of features, in the form of prominent peaks. The features are unique to a material and can be used as a fingerprint to identify the material. Thus, a reference database of Raman spectra of materials is enough for the identification of a material. However, a full understanding of the vibration is required to get a complete picture of properties from the Raman spectrum.

Variations observed in the features can range from changes in the Raman intensity, full width half maximum (FWHM), or the frequency shifts of the peaks with respect to the ideal material's Raman spectrum. Traditionally, these changes can be attributed to the change in amount of material, crystallinity or internal stresses in the sample.

Using a focused spot of laser as the primary excitation beam, a spatial map of Raman spectra can be obtained for a macro sized sample by systematically moving the stage in steps and measuring the spectrum (rotation is not allowed). Such Raman spatial maps can carry information pertaining to local composition, crystallinity and stress changes in a material.

2.2.1.3 Angle Dependent Raman

Traditionally, the inherent ability of a commercial instrument to measure angle dependent Raman is rare. This ability is usually provided by offering the ability to polarize incident light in the instrument. In this instrument, the polarizations offered by the names normal and orthogonal are in the directions. In the normal setting, there is no additional waveplate used, and the light is polarized along the x-axis of the stage (horizontal). On the other hand, the orthogonal arrangement uses a half-waveplate and the incident laser is polarized along the y-axis (vertical direction), as shown in the figure 4.

However using the modifications mentioned below, Raman spectra on crystalline material (TiS_3 and ZrS_3) was recorded at the same spot for various angles. A 10 degree step was used to plot polar spectra for both normal and orthogonal arrangements. Visualization of the raw data was done using contour plots (or 3D raman plots)

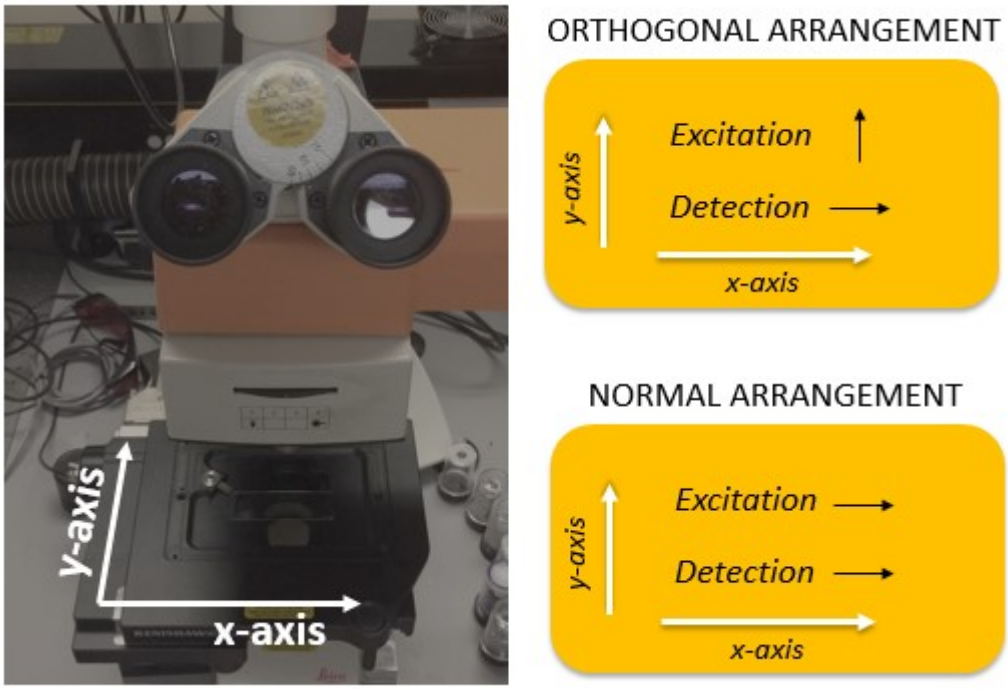

Figure 4. Figure showing schematics for Normal and Orthogonal arrangements.

consisting of angle on the y-axis, Raman shift on the x-axis and a rainbow color band for the intensity.

For easier interpretation of this data, Raman spectra for each angle step was then fit to appropriate number of Gaussian functions to obtain the peak positions, peak areas and intensities at the peak. One of these three parameters on the y-axis, polar plots were plotted.

Polar plots obtained throughout these experiments were either symmetrical-four-lobed, elliptical , asymmetric-four-lobed, or two-lobed. Where the latter three, owing to their 180 degree periodicity (absence of the traditional 90 degree periodicity), are proposed to indicate in-plane anisotropy of Raman modes.

2.2.1.4 Equipment and Modifications

The device used for Raman spectroscopy in this study was Renishaw InVia confocal microscope. This reflection microscopy instrument was equipped with objective lenses 5x, 20x, 50x and 100x with a numerical aperture of 0.75 for Raman imaging. We use the visible 15 mW, 488 nm laser as the incident beam which allows imaging of Raman shifts within 100 cm^{-1} of the excitation energy. At the highest magnification the instrument has a spatial resolution (beam spot size) of 1 μm. A grating of 1200 l/mm was used. An automated mechanical stage allows the movement of sample with extremely fine accuracy, to record spatial maps.

To record the trend of changes associated with Raman spectra with the incident angle of polarized laser without inflicting change to the incident beam, a stage that allows rotation had to be installed. A manual rotation stage was installed onto the automatic stage using double sided tape (shown in figure 5). Although step sizes of 10 to 20 degrees can safely be interpolated to obtain the general trend, this stage allows the alignment of polarized incident light in steps of less than 1 degree with respect to the sample crystalline direction.

2.2.2 Photoluminescence (PL) Spectroscopy

When a material is excited by an electromagnetic beam such as laser, both Raman scattering and photoluminescence (PL) can occur. In fact, the latter can have a yield which is several times stronger than the former. Since the same equipment as Raman was used to record the photoluminescence spectra, it inherently has all of the positives that are associated with the Raman spectroscopy – an efficient, non-contact,

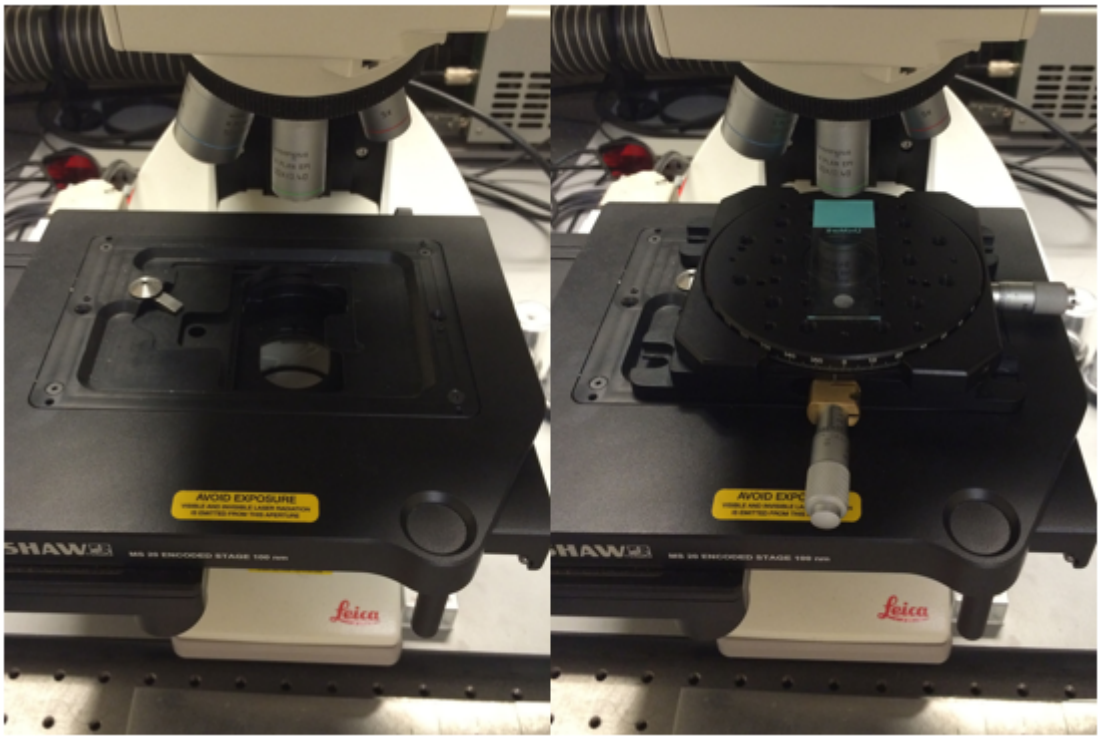

Figure 5. Comparative images of the stage without and with the rotation stage.

non-destructive and a widely used technique for the analysis of semiconductors with stimulating optoelectronic properties.

2.2.2.1 Photoluminescence

Photoluminescence is defined as the spontaneous emission of light from a material under optical excitation. Photoluminescence in certain photoluminescent material can be observed by exciting the material using an incident laser beam which has an energy larger ($h\nu$) than the bandgap (E_G), enough to excite carriers from the valence band to the conduction band. The resulting photons reemitted materials are then captured using a CCD detector.

The emission recorded from the material is then used to extract out a variety of

information detailing the discrete electronic states involving the material's intrinsic optical processes. Besides, PL spectra can also be used to understand the transitions associated with endemic defects in semiconductor materials.

This energy of the emitted photons is measured in energy and a unit of electronvolts (eV) is suitably used. We use grating and a CCD detector to estimate the count of emitted photons at a particular energy. The spectra is graphically depicted in our measurements as PL spectra. In this spectra, the intensity (photon count) of the scattered light (y-axis) is plotted for energy (eV) on the x-axis.

2.2.2.2 Standard Information From the Spectra

Since PL spectra is amenable to radiative processes, it is very hard to study indirect bandgap materials which have very weak radiative activity. Also, recombination mechanisms at deep centers where radiative transitions give very broad spectra due to strong phonon coupling are also hard to study.

Firstly, the PL spectra can be used to determine the intrinsic optical bandgap of a direct bandgap semiconductor. The recombination in a direct bandgap semiconductor, which has intrinsic valence band maximum (VBM) and conduction band minimum (CBM) at the same momentum value, is very efficient process. Thus they are very photoluminescent and will show a large peak at an x-axis value E_G. The peak position of the PL spectra obtained in a defect free direct band gap semiconductor can be said to be its optical bandgap.

Secondly, the material quality of a sample can be assessed by comparison of the PL yield of the sample with an ideal direct bandgap material with maximum yield. The radiative yield (PL) for a defective sample would be a smaller because of the presence

of a significant amount of non-radiative recombination, which is often associated with localized defects in the sample.

Similarly, radiative transitions from localized defects and the photoluminescence energy associated to these levels can be used to identify the specific type of defects, or doping in the material.

Low temperature PL studies has its own advantages too. Underlying contributions to the main PL peak at room temperature can be deconvoluted into components from various transitions at low temperature.

2.2.2.3 Power Dependence PL

To further obtain the underlying reason for emission at different energies, PL spectra obtained by varying the power of the excitation laser can be crucial. In this equipment, the power of the initial laser beam, 15 mW can be controlled using a linear analogue knob. For consistency, the knob is maintained at 50%, thus 7.5 mW of the laser power is used. Furthermore, the power can be cut down through filters (allowing 100%, 50%, 10%, 5%, 1%, 0.5%, 0.1%, 0.05% and so on) selected via the software (Renishaw Wire).

For the interpretation of the data obtained via various filters at the same spot on the sample, the spectra are fit to Gaussian functions, peak positions and areas (integrated PL intensity) of PL peaks are obtained at different powers. Then, one of these parameters (y-axis) are plotted against the absolute laser power (mW on y-axis).

As specified in the literature [71], with increase in the laser excitation power, PL intensities from bound excitons (from defects) tends to saturate towards higher powers. This happens as defects get fully populated with excitons. Whereas the

integrated intensity of the PL peak associated with free excitons (band to band) shows no saturation and scales almost linearly with power. Thus, at lower powers the overall PL spectrum is dominated by the bound excitons and at higher powers the PL peak from free excitons dominates [71].

2.2.2.4 Angle Resolved PL

Analogous to aforementioned angle dependent Raman, angle resolved PL (ARPL) measurements can be recorded by turning the stage manually both in orthogonal and normal geometries.

Using the modifications mentioned before, PL spectra on crystalline material (ZrS_3) was recorded at the same spot for various angles. A 20 degree step was used to plot polar spectra for both normal and orthogonal arrangements. Visualization of the raw data was done using contour plots consisting of angle on the y-axis, energy (eV) on the x-axis and a rainbow color band to represent the intensity.

For easier interpretation of this data, PL spectra for each angle step was then fit to an appropriate Gaussian function to obtain the peak positions, peak areas and intensities. Using one of these three parameters on the y-axis, polar plots were plotted. Polar plots of area vs angle obtained from ZrS_3 from the experiments were always two-lobed, indicating in-plane anisotropic luminescence.

2.2.3 X-ray Diffraction

X-ray powder diffraction (XRD) is a quick analytical technique which is primarily used to obtain unit cell information, phase identification and crystallite size of a

crystalline material. In a simplified picture, an XRD incidents a collimated monochromatic beam of x-rays on a crystalline sample for a range of angles (2θ). For x-ray wavelengths close to the crystal plane spacing, the crystal acts as a 3D diffraction grating and allows constructive interference of the reflected beams in a few directions. A detector records and processes this reflected X-ray beam intensity and converts it to a count rate which is then output on the computer screen in form of a intensity vs angle (2θ) plot. For particular 2θ values for which the constructive interference happens, peaks appear in the plot.

2.2.3.1 Theory

For the primary x-ray beam wavelength of λ the angles (θ_{hkl}) that produce a constructive interference from the corresponding (hkl) crystal plane which is at a distance of d_{hkl} is given by the Braggs law:

$$n\lambda = 2d_{hkl}sin\theta_{hkl} \tag{2.1}$$

Here, n is the order of the reflection. And d_{hkl} is a function of the lattice parameters of the crystal. Since both ZrS_3 and TiS_3 are monoclinic crystals, the equation to calculate d-spacing for a monoclinic crystal is given by:

$$\frac{1}{d^2} = \frac{1}{sin^2\beta}\left(\frac{h^2}{a^2} + \frac{k^2sin^2\beta}{b^2} + \frac{l^2}{c^2} - \frac{2hl\ cos\beta}{ac}\right) \tag{2.2}$$

The d_{hkl} from each peak can thus be matched with the d_{hkl} obtained from the equation 2.2 defined for monoclinic cells, with hkl and lattice parameters obtained from the XRD card for the respective material. This way, phase can be matched despite missing peaks in the database card.

2.2.3.2 Experimental

The XRD spectrum for both ZrS_3 and TiS_3 crystals were recorded on Siemens D5000 x-ray diffractometer machine which uses a Cu K_α radiation with $\lambda = 1.54$ Å. About 100 mg of crystals were placed in a straight line on a zero background plate so as to maximize their exposure to the incident x-ray beam. Scan rates of 5 degrees per minute were used for 2θ ranging from 15^o to 60^o.

Chapter 3

ZIRCONIUM TRISULPHIDE - ZrS_3

3.1 Crystal Structure

Zirconium Trisulphide (ZrS_3) crystalizes in a typical monoclinic cell, with α, $\gamma = 90^o$ and $\beta \neq 90^o$. To visualize the structure, images of several lattices (2 in the a direction, 8 in the b direction and 1 in the c direction) have been shown in the figure 6 a, b and c as seen from axes a [100], b [010] and c [001] respectively. The figure 6 d, represents 2 layers of ZrS_3 stacked and coupled via the van-der-Waals forces. The green spheres represent the Zirconium atom and the yellow ones represent the Sulphur atoms. While the dotted black lines show the primitive lattice.

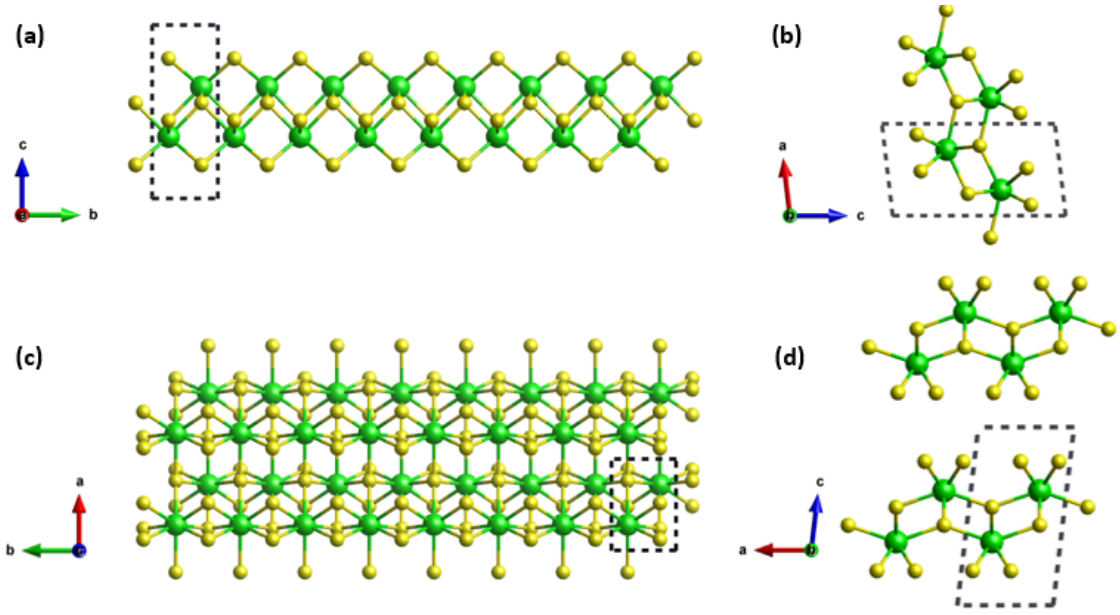

Figure 6. Crystal structure of ZrS_3.

In the crystal structure for ZrS_3, the Zr-S bond length between the Zr atom and S atom inside the trigonal prism chain is 2.63 Å, while Zr-S bond length between the Zr atom inside the trigonal prism and S atom of the adjacent chain is 2.75 Å. This suggests weaker bonding between adjacent chains. Wieting et al. [72] propose a central force model based up on their Raman data which estimates the coupling strength between Zr-S bond between adjacent chains is approximately one-fifth of the Zr-S bond within the chain. This reflects in the high-aspect ratio (b-axis : a-axis) elongated rectangular shapes in optical images of exfoliated ZrS_3. Hence the name, quasi one-dimensional crystal. During the experiments crystals were consistently observed to be wire-like flakes with a rather high aspect ratio.

In summary, the coupling in c direction is the weakest (van-der-Waals), followed by the intra-layer coupling between adjacent chains (a-axis) and the coupling in the b-axis is the strongest. This explains why exfoliated crystals of ZrS_3 appear as elongated rectangular flakes with high aspect ratio (b-axis : a-axis), seen in Figure 7.

3.2 Growth

The ZrS_3 crystals were grown using the CVT synthesis method as described in the chapter 2. Jin et al. [70] propose optimum parameters for CVT growth of ZrS_3 nanobelts. The crystals of ZrS_3 formed as a result of CVT through the reaction between Zirconium foil (Sigma Aldrich, 0.01 mm thickness, 99.98%), and sulfur flakes (Sigma Aldrich, 99.99%). Reactants were weighed in a molar ratio of (Zr : S, 1 : 3.5). The complete mixture of 500 mg was transferred to one end of a quartz-glass tube of 10 mm diameter and 150 mm length and then the glass tube was evacuated and sealed.

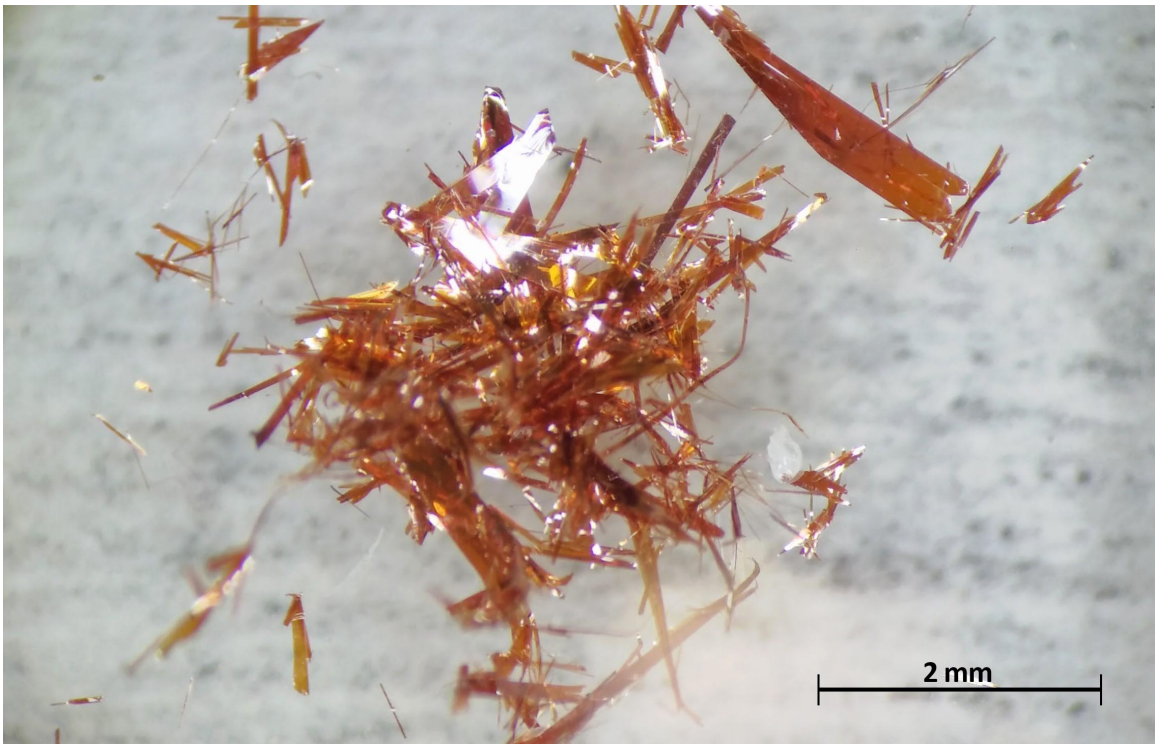

Figure 7. Crystals of ZrS_3 grown using CVT.

CVT was done using a Thermo Scientific Lindberg Blue M Tube Furnace with three zones, however the sealed tube placed inside a larger quartz tube covered only two zones of the furnace. The hotter end, with the reactants, was maintained at 600 ^{o}C and the colder end was maintained at 520 ^{o}C. For safety reasons, the temperature was ramped from room temperature to the growth temperature in 24 hours. The growth temperature was maintained for 90 hours and then the furnace was let to cool naturally.

Crystals obtained as a result of this growth had a reddish hue and were shaped like whiskers. The size of crystals was fairly large and the largest ones were about 1-3 mm in length as seen in Figure 7.

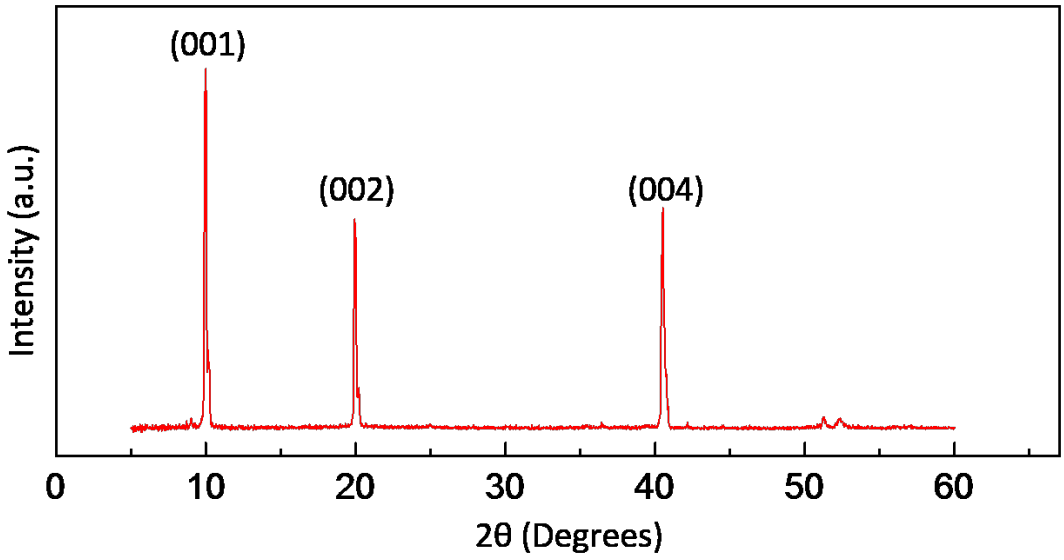

Figure 8. Powder XRD data of macro ZrS_3 crystals.

3.3 XRD Data

As per the settings used for the collection of XRD data mentioned in the methods section (chapter 2), the XRD-pattern obtained has been shown in figure 8. It is to be noted that the pattern was obtained from the macro sized belts of ZrS_3 with the c-axis facing upwards on the zero background plate. Thus, the pattern appears significantly different (with far fewer peaks) than any ZrS_3 data present in the XRD database. Here, only the planes perpendicular to the c-axis were probed, which is sufficient for our purposes to verify the phase of this material.

From the International Centre for Diffraction Data (ICDD) card number 00-015-0790, the (001) and (002) peaks show a good match. The lattice parameters obtained are: a = 5.123 Å, b = 3.627 Å, c = 8.986 Å, and $\beta = 97.15^o$. Suggesting that ZrS_3 crystallizes in a monoclinic cell of $P2_1/m$ space group with lattice constants as

mentioned. However, the peak at $2\theta = 40.5^o$, was found to be missing from the card data.

Using equations 2.1 and 2.2 for this monoclinic crystal and substituting the values 0, 0, 4 for h, k, l respectively, the peak at $2\theta = 40.5^o$ was verified from the plane data of the ICDD card and labled as (004).

3.4 Raman Spectra

As discussed above, ZrS_3 crystallizes in a monoclinic cell of space group $P2_1/m$. The primitive unit cell consists of 8 atoms. And the mechanical representations can thus be decomposed into 8 x 3 irreducible representations. These can be represented as:

$$\Gamma_{crystal} = 8A_g + 4A_u + 4B_g + 4B_u \tag{3.1}$$

While, for a single chain where the unit cell consists of 4 atoms, it can be writte as:

$$\Gamma_{chain} = 4A_1 + 4B_1 + A_2 + 3B_2 \tag{3.2}$$

These modes can further be correlated to a set of atomic vibrations perpendicular and parallel to the ZrS_3 chains. It has been shown previously that the atomic vibrations correlated with the A_u & B_g modes for the crystal, A_2 & B_2 for the chain, are parallel to the chains, or along the b-axis. While the modes correlated with A_g & B_u for the crystal and A_2 & B_2 for the chain, are perpendicular to the chains. Out of the 21 k = 0 modes, twelve of these mode are Raman active ($8A_g$ and $4B_g$), while 9 are infrared active (A_u and B_u) [73].

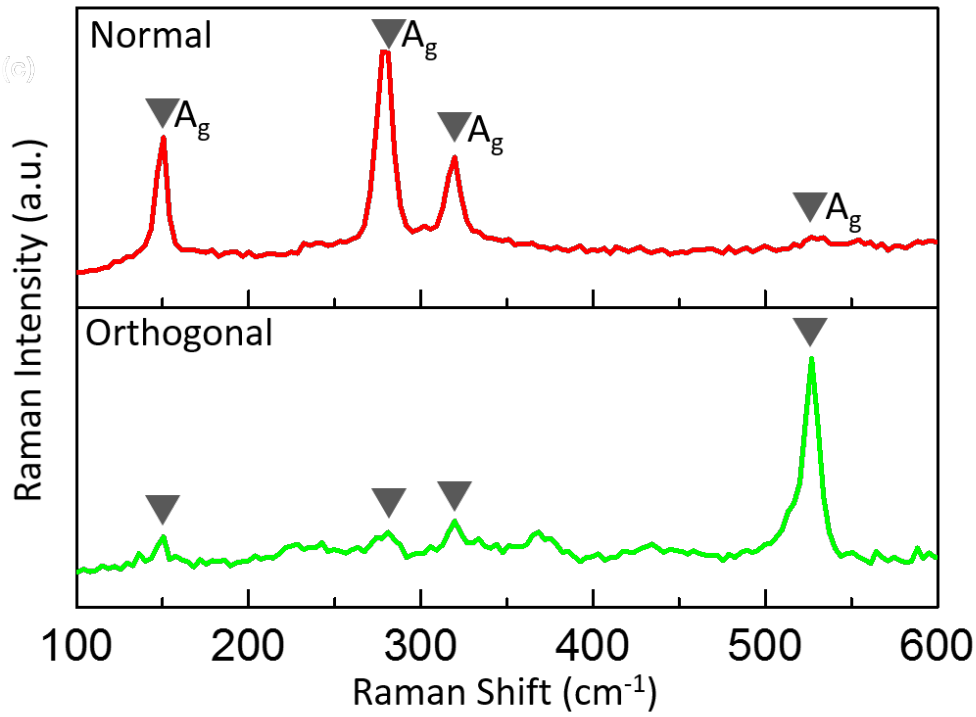

Figure 9. Raman spectrum for exfoliated ZrS_3 crystals on sapphire.

Consistent with previously shown Raman spectra for ZrS_3, our crystals show peaks at 150.5 cm^{-1}, 277.6 cm^{-1}, 319.6 cm^{-1} and 527 cm^{-1}. Just four peaks appearing instead of the 12 active modes is probably suggests higher symmetry of undistorted chains [67] or degenerate peaks. Specifically, when measured in the normal configuration, the 150.5 cm^{-1}, 277.6 cm^{-1}, 319.6 cm^{-1} peaks are prominent, while the 527 cm^{-1} peak is significantly weaker in intensity, while their intensities are lower and higher, respectively, in orthogonal configuration (shown in figure 9).

When measuring Raman spectrum in the back-scattering geometry, from Loudon's [74] polarisability tensors it is known that, A modes are allowed in normal configurations and B modes are allowed in orthogonal scattering conditions. Using this

argument, the peaks 150.5 cm^{-1}, 277.6 cm^{-1}, 319.6 cm^{-1} are labled as A_g, while the peak at 527 cm^{-1}, which appears prominent only in cross (orthogonal) configuration is still actually less intense than any of the major peaks in normal configuration. It is only relatively stronger as compared to other peaks in orthogonal configuration. So, it is still an A_g peak.

Further, it should be noted that the lowest frequency mode of 150.5 cm^{-1} has previously been attributed to a "rigid-chain mode". Similarly, the latter 277.6 cm^{-1}, 319.6 cm^{-1} peaks were attributed to Zr-S inter and intra chain vibrations. While the 527 cm^{-1} peak have been shown to originate from the stretching of the $(S–S)^{2-}$ group, and the shoulders around 527 cm^{-1} may have originated from an isotopic effect of S (which is naturally abundant at 4.2%) according to previous reports [75, 76].

3.5 Angle Dependent Raman Spectra

As described in the methods section of Chapter 2, the angle resolved Raman spectra was measured for an ideal flake in both orthogonal and normal configurations. The sample was placed on a rotating stage and Raman data was captured at the same location for every 10 degrees from 0 to 360 degrees. A 3 dimensional plot of raman spectra versus the angle of the flake has been shown in the figures 10 and 12 for orthogonal and normal arrangements, respectively.

In the angle dependent raman measured for orthogonal arrangement as seen in figure 10, a 180 degree periodicity can be observed for the intensities of the Raman peaks. The maxima for all four peaks occurs at 90 and 270 degrees, while the minima is occurs at 0 and 180 degrees. To demonstrate the variation of intensities clearly, the

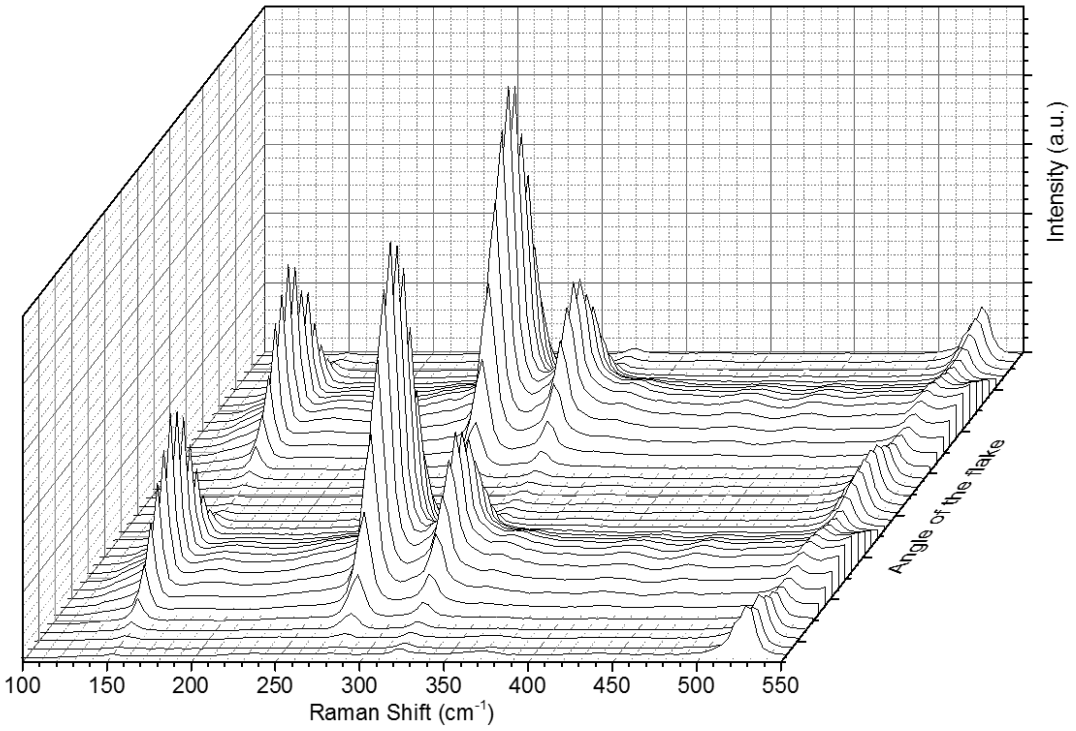

Figure 10. 3D angle dependent Raman plot in orthogonal arrangement for ZrS_3.

raman intensities of all the peaks 150.5 cm^{-1}, 277.6 cm^{-1}, 319.6 cm^{-1} and 527 cm^{-1} have been shown in the polar plot - figure 11. Again it can be seen that a two lobed plot is the prominent feature of all the peaks. This intensity variation is a lot like how PL varies with angle, and can be considered as a behaviour from an anisotropic material.

The angle dependent raman measured for normal arrangement shows a significantly different and surprisingly unexpected behaviour. As seen in figure 12, a 90 degree periodicity can be observed for the intensities of the Raman peaks. The maxima for

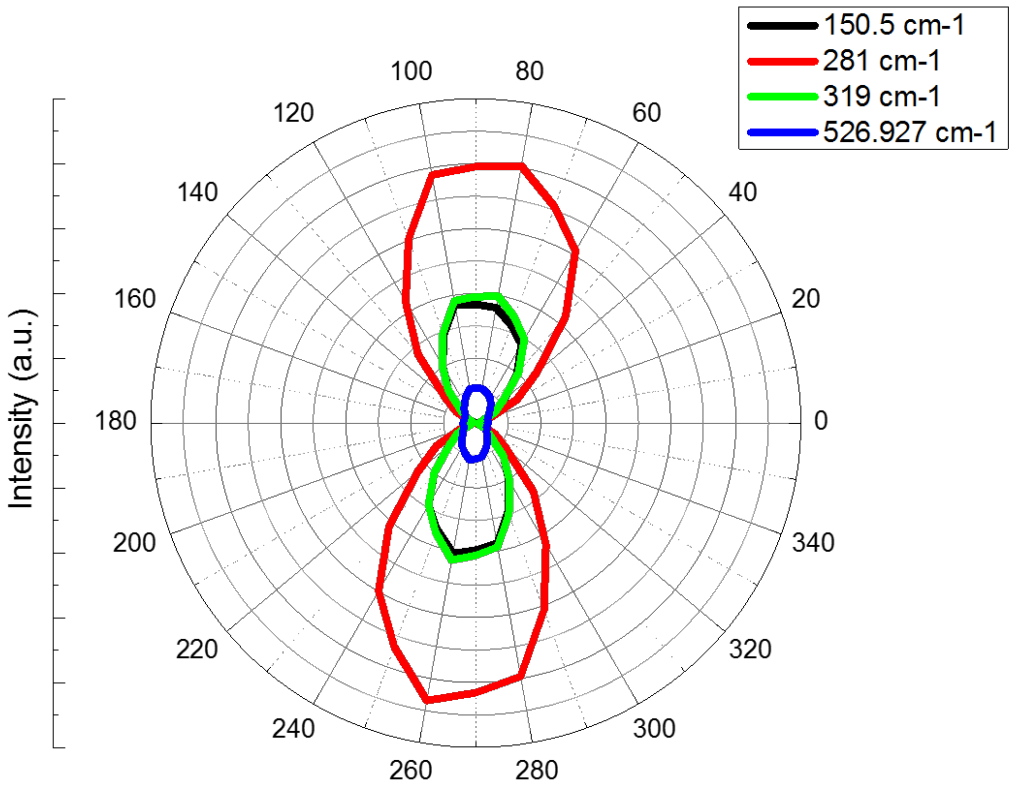

Figure 11. Polar plot of angle dependent Raman in orthogonal arrangement.

all peaks is reachd four times in the span of 0 - 360 degrees. For all four peaks, the maxima occurs at 45, 135, 225 and 315 degrees, while the minima is occurs at 0, 90, 180 and 360 degrees. To demonstrate the variation of intensities clearly, the raman intensities of all the peaks 150.5 cm^{-1}, 277.6 cm^{-1}, 319.6 cm^{-1} and 527 cm^{-1} have been shown in the polar plot - figure 13. It can be seen that a four lobed plot is the prominent feature of all the peaks.

Unlike PL intensity, raman intensity (I_r) is dictated by the raman tensor (R), rather than the electric field directly. If E_i and E_r are incident and scattered polarization vectors, then $I_r \propto |E_i.R.E_s|^2$ [60]. Whereas the PL intensity is directly a meausure of

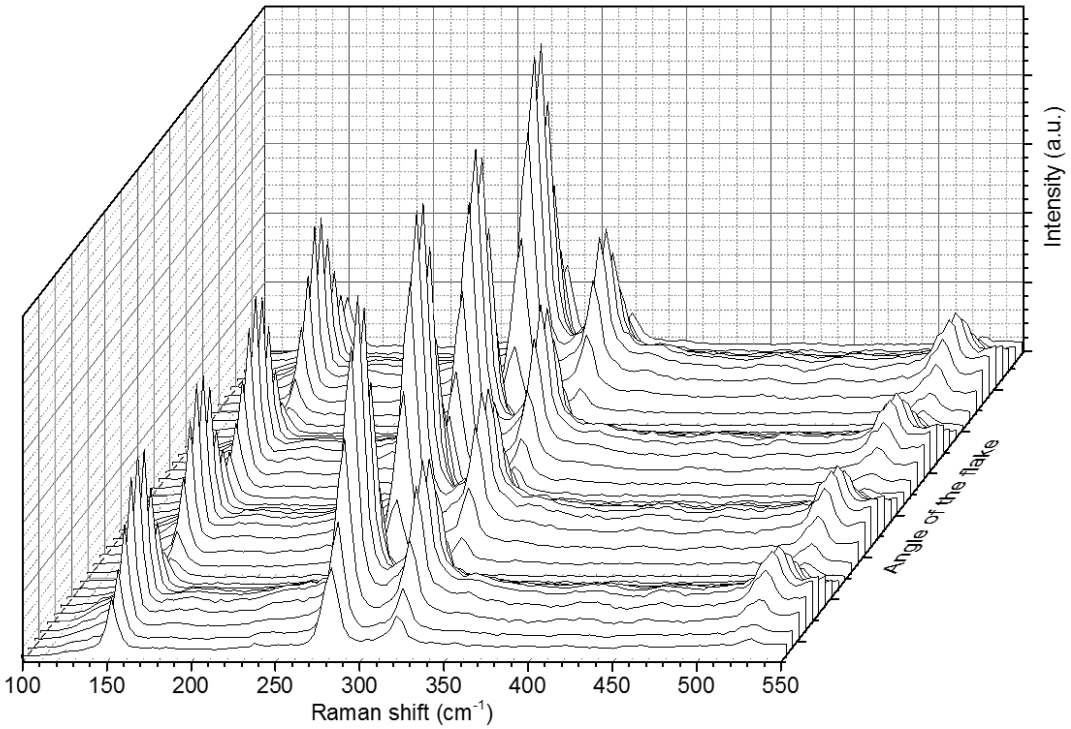

Figure 12. 3D angle dependent Raman plot in normal arrangement for ZrS_3.

the square of induced electric field in the flake. Hence, the raman in normal setting shows an unexpected behaviour. The discussion of specific Raman tensor behaviour for individual peaks is beyond the scope of this thesis. Further studies are required to clearly understand the angle dependent raman behaviour of ZrS_3 crystals, especially in the normal configuration.

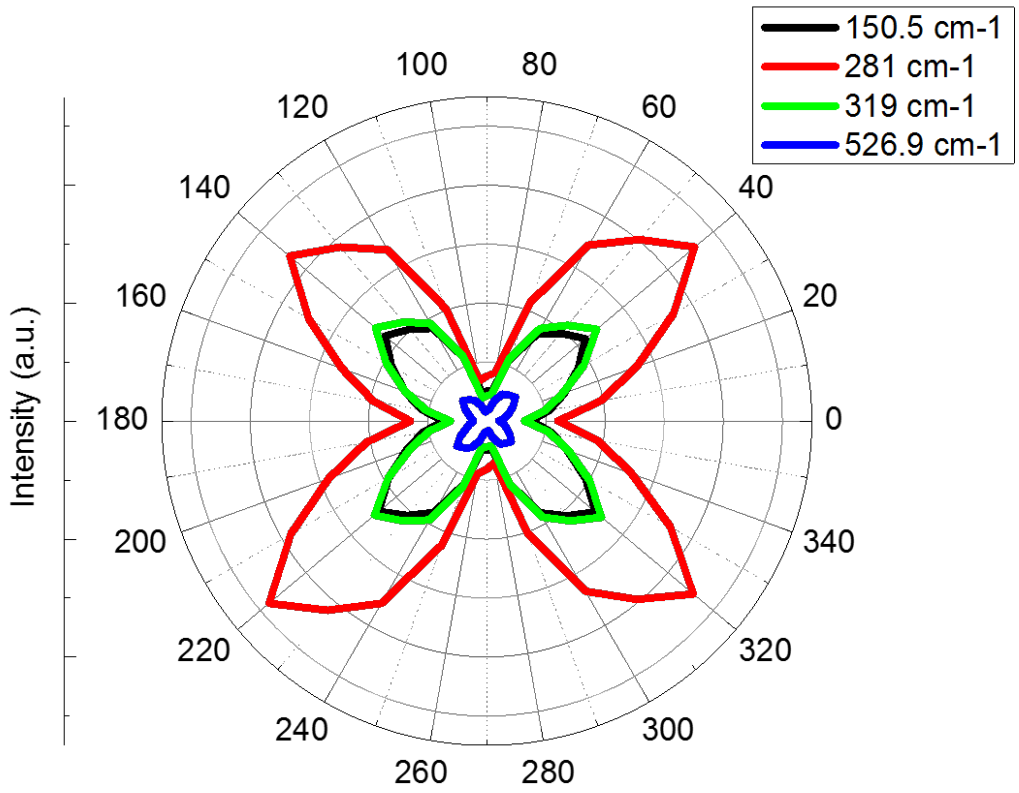

Figure 13. Polar plot of angle dependent Raman in Normal arrangement.

3.6 Band Structure and Photoluminescence Spectra

According to HSE06 [77] calculated electronic band structure of ZrS_3 as shown in figure 14, it is an indirect band gap semiconductor with a band gap of 1.88 eV. For a sulphur vacancy, our calculation showed a peak in density of states about 0.59 eV below the conduction band minima (CBM), or 1.29 eV above the valence band minima (VBM). These results are significantly different from what has been calculated in the literature previously. Recently, Jin et al.[78] have calculated a band gap of 1.83 and 2.13 for indirect and direct band gap transitions for bulk ZrS_3. Previously, absorption

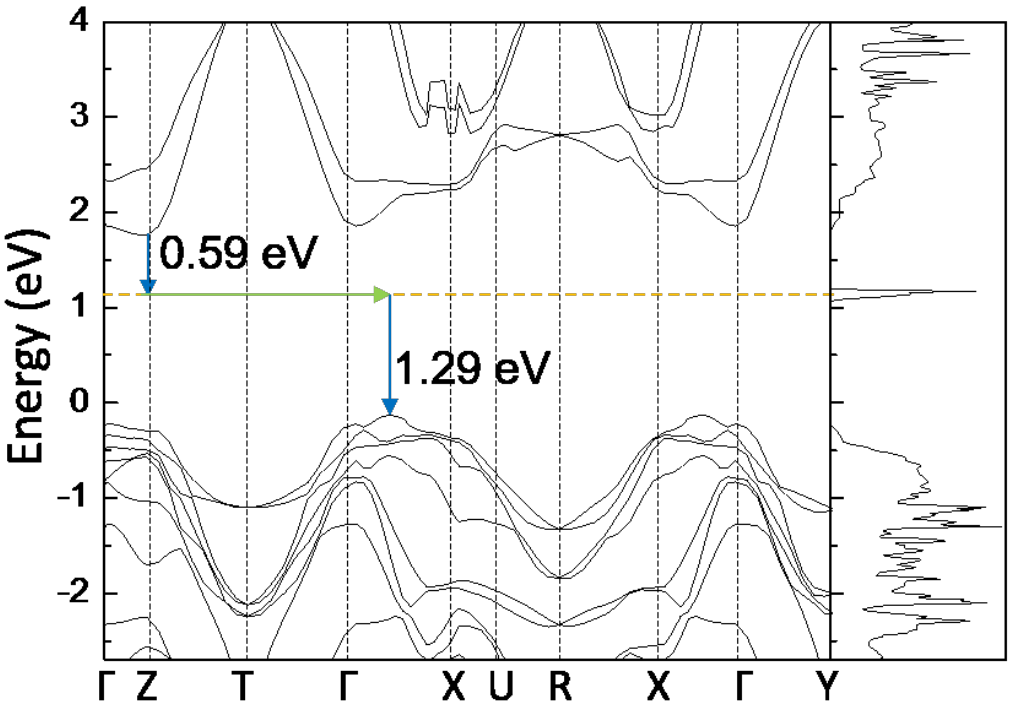

Figure 14. Band structure of bulk ZrS_3 calculated using HSE06.

studies on ZrS_3 have shown a direct band gap transition in ZrS_3 at 2.055 eV (for E || b) and 2.085 eV (for E $\perp$ b).

The PL measured was at very low laser power - 0.75 mW, so as to not damage the sample because of heating. The spectra from a typical flake showing both peaks appears as shown in figure 15. At room temperature the PL spectra of thick exfoliated layers of ZrS_3 on sapphire showed a relatively inconsistent PL in terms of intensity of 1.45 eV peak. However, the other peak at 1.8 eV consistently appeared in all samples. A fairly broad and inconsistent peak at 1.45 eV and another broad one at 1.8 eV were found to be common features for several flakes. Their high FWHM indicates the involvement of phonons in both the transition processes.

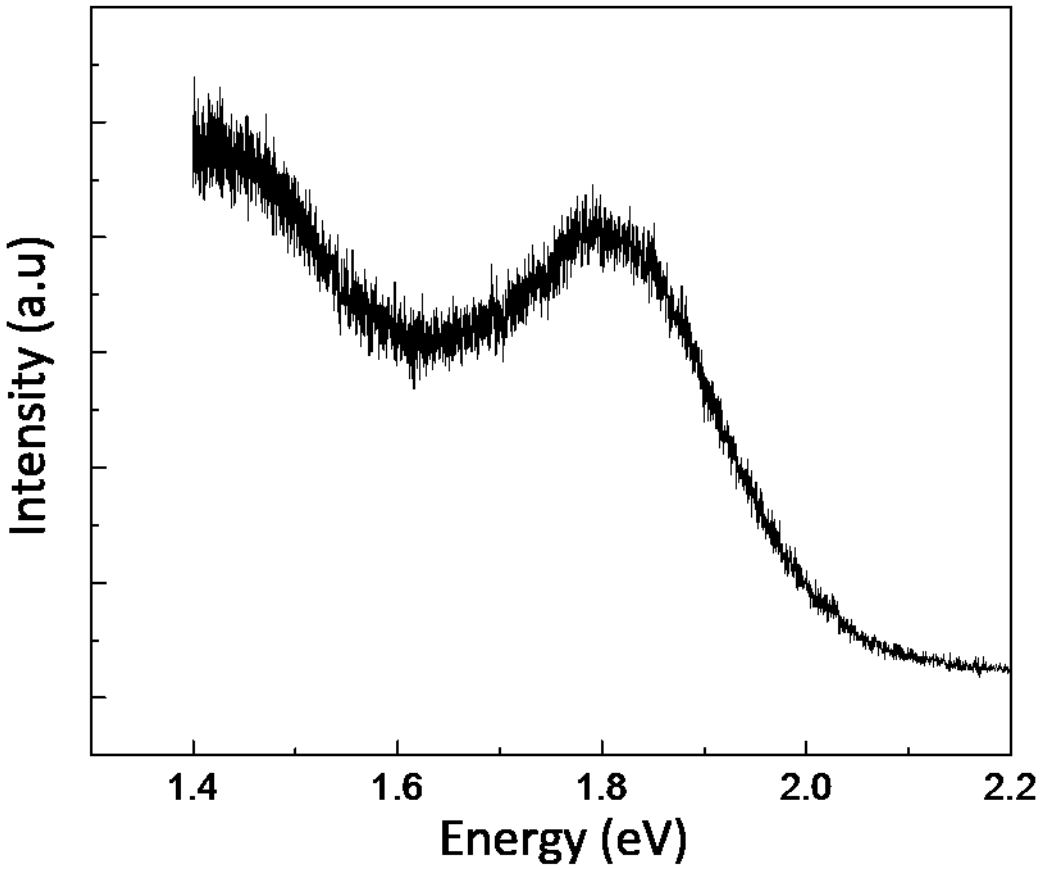

Figure 15. PL spectra of an exfoliated ZrS_3 crystal at room temperature.

To judge the origin of these two peaks, power dependence PL was conducted on various samples. The results from a representative sample have been discussed in the following section.

3.7 Power Dependence PL

The PL power dependence was measured for an initial laser power of 7.5 mW, which was consequently cut down using filters to 0.05, 0.1, 0.5, 1, 5 and 10 % of 7.5

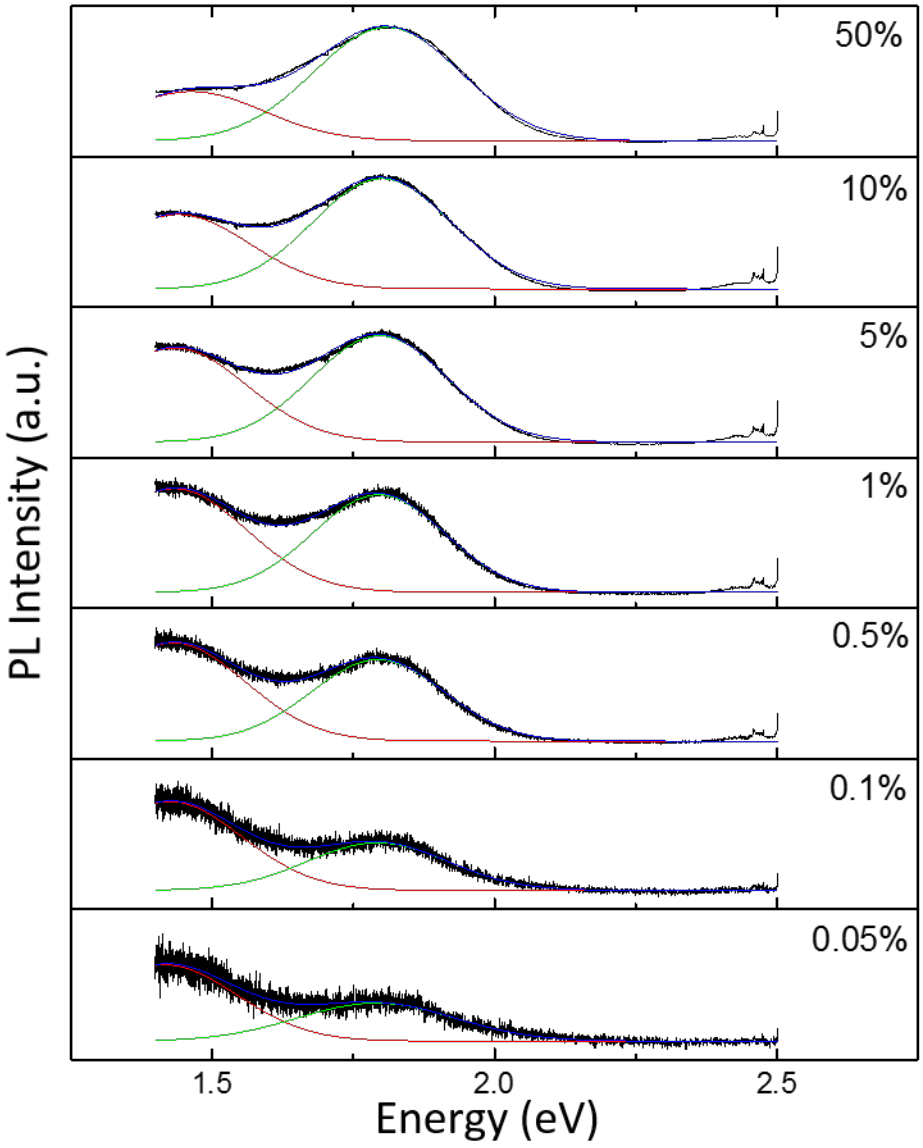

Figure 16. PL spectra of an exfoliated ZrS_3 crystal at room temperature for various laser powers.

mW. It can clearly be seen in the figure 16 that the peak at 1.45 eV is dominating in the low power regimes. However, as the power increases (going up), the peak at 1.45 eV appears saturated and the 1.85 eV peak takes over the spectrum.

If the peaks at 1.45 eV and 1.8 eV are individually fit using gaussian functions and their respective areas are plotted against the absolute laser power in milliwatt (mW), the trend can clearly be observed. Figure 16 shows the independent gaussian functions for 1.8 eV peak is shown in green line and 1.45 eV peak shown in red line. In figure 17 it is observed that the integrated PL intensity of the 1.45 peak (shown in red) gradually starts saturating at higher powers of excitation laser. However, the integrated PL intensity of 1.8 eV peak (shown in green) does not show any sign of saturation even at 10% laser power.

This can also be observed in the inset (in log-log scale) that the peak at 1.8 eV has a slope of 0.91, which is close to 1.00, meaning the transition gives back the same number of photons as it absorbs, indicating a band to band transition, or a transition from a densly populated impurity band to the valence band edge. Whereas the slope of the 1.45 eV peak in the log-log scale plot is close to one, indicating gradual saturation - which is a strong indicator that this transition happens from a bound exciton.

3.8 Angle Resolved PL

Angle resolved PL was measured for an ideal flake with a weak 1.45 eV peak and a dominant 1.8 eV peak. The sample kept on a rotating stage was rotated by 20 degrees and a PL spectra was recorded from angles 0 to 360 degrees. This was done for both orthogonal and normal configuration (defined in chapter 2) of the equipment.

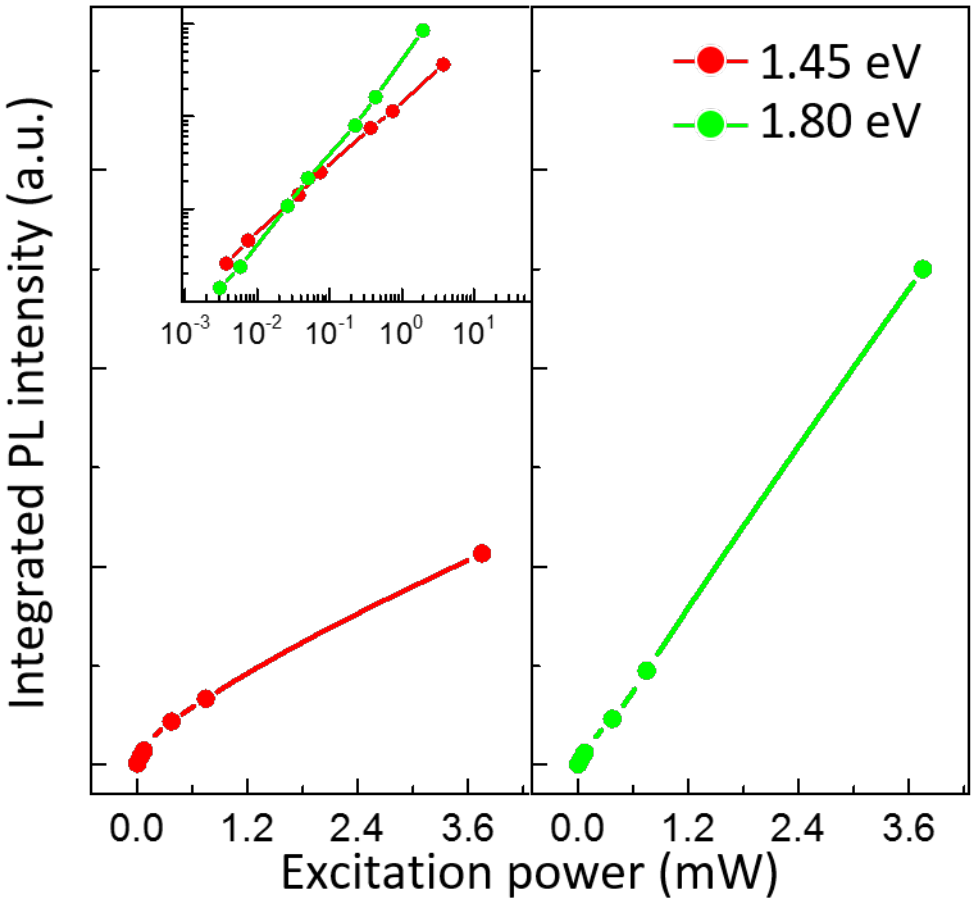

Figure 17. PL peak area vs. absolute laser power for ZrS_3 crystal at room temperature, in linear-linear scale (inset log-log scale).

In order to visualize the raw collected data, contour plots for orthogonal and normal arrangements are shown in the figure 18 and 19.

In the orthogonal arrangement (figure 18) it is clearly seen that the PL intensity reaches a maxima at angles 270 and 90 degrees. These flake angles in orthogonal arrangement are also the position of the flake where the polarization of incident laser direction is along the b-axis - showing the luminescence is the highest when the E-field of incident light is aligned parallel to the b-axis (or the chain direction). Similarly, a minima in PL intensity is reached when the flake angle is 0 or 180 or 360 degrees. Suggesting that the luminescence is weakest when the E-field of the incident laser is aligned perpendicular to the chain direction (or in the a-axis direction).

In the Normal arrangement (figure 19) it is clearly seen that the PL intensity reaches a maxima when the flake's angle is 0 and 180 and 360 degrees. These flake angles in normal arrangement are also the position of the flake where the polarization of incident laser direction is along the b-axis - Again, showing the luminescence is the highest when the E-field of incident light is aligned parallel to the b-axis (or the chain direction). Similarly, a minima in PL intensity is reached when the flake angle is 90 or 270 degrees. Suggesting that the luminescence is weakest when the E-field of the incident laser is aligned perpendicular to the chain direction (or in the a-axis direction).

While true for the maximum intensity, the same trend can also be seen in the polar plots where y axis of each point in the plot represents the integrated PL intensity of the PL at that angle. A clear anisotropic behaviour of the crystal in terms of total luminescence is observed. For comparison purposes, in figure 20 a red line represents

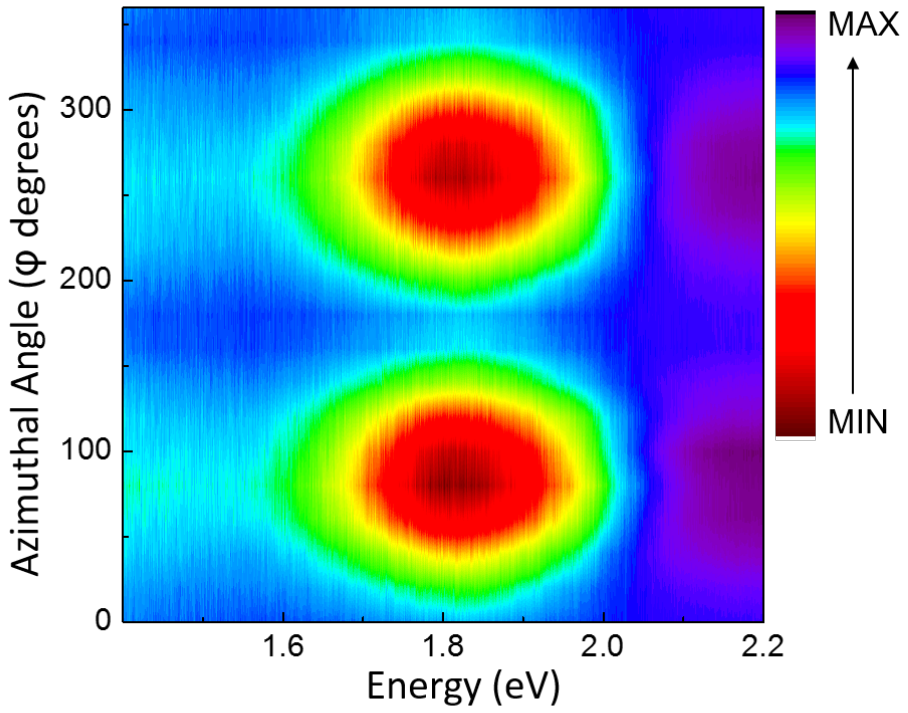

Figure 18. Angle resolved PL in orthogonal configuration.

the angle resolved PL measured for a monolayer of MoS_3. It is evident that shows little or no variation in the PL intensity with respect to the angle of the flake.

Just as observed in the contour plots, the integrated area PL area follows the same trend. For orthogonal geometry (shown in figure 20), it reaches a maxima at 270 and 90 degrees where the E-field of the incident laser is aligned along the b-axis. And reaches a minima for 0 or 180 or 360 degrees, where the E-field of the incident laser is aligned perpendicular to the b-axis.

Also in the normal configuration (shown in figure 20), the integrated area PL area follows the same trend as seen in the raw data contour plots. For normal geometry,

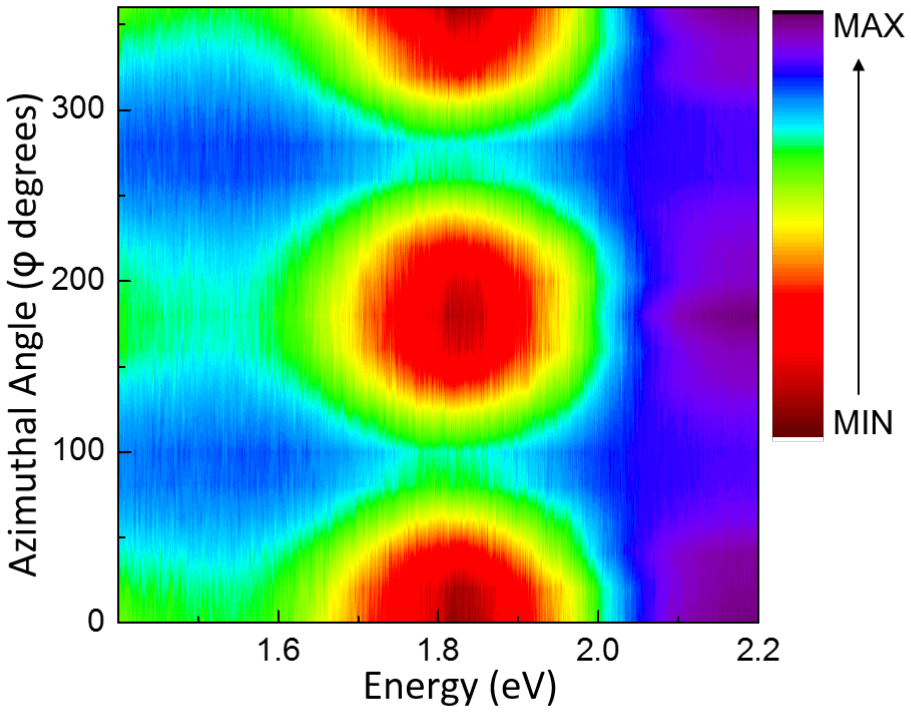

Figure 19. Angle resolved PL in normal configuration.

the PL integrated area reaches a maxima at 0, 280 and 360 degrees where the E-field of the incident laser is aligned along the b-axis. And reaches a minima for 90 and 270 degrees, where the E-field of the incident laser is aligned perpendicular to the b-axis.

3.9 Discussion

Since the crystal structure of ZrS_3 is anisotropic in the planar direction perpendicular to the c-axis. So, naturally this geometric anisotropy is expected to influence

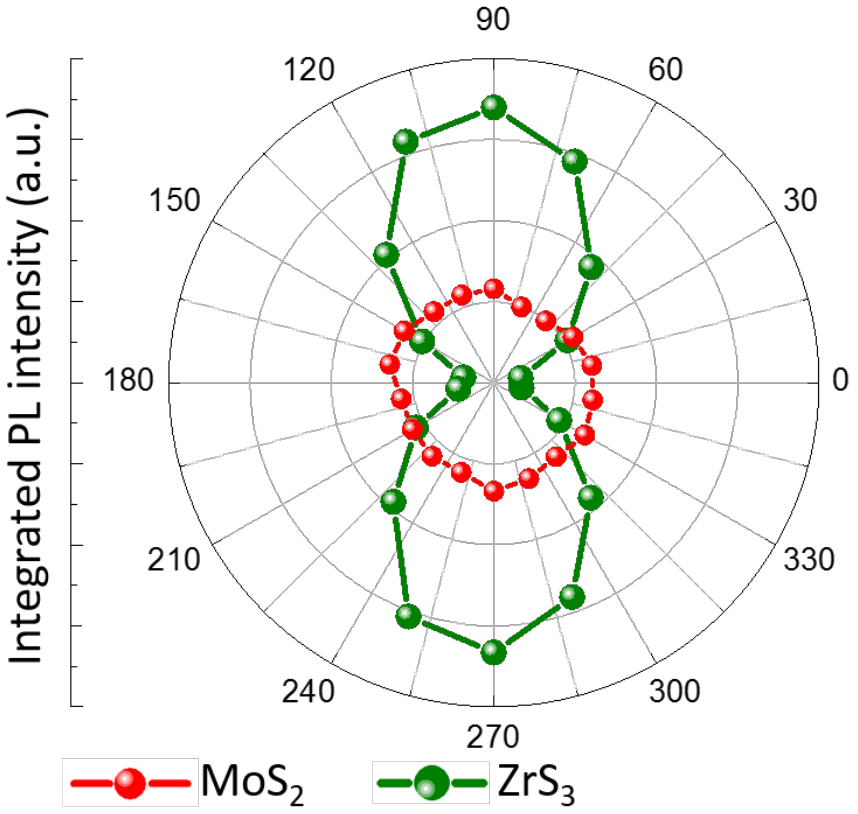

Figure 20. Polar plot of integrated area versus azimuthal flake angle for angle resolved PL in orthogonal configuration.

the properties of the material. But what exactly is the cause of the anisotropic PL emission as shown in the angle resolved measurements?

The answer lies in the classical electromagnetic theory. As previously shown by Fang et al. [79] and Rivas et al. [80] that the behaviour of purely one dimensional nanowires, such as ZnO or other semiconducting nanowires, exhibit strong optical anisotropy too.

Here, in ZrS_3, let us consider one of the ZrS_6 trigonal prismatic chain running along the b-axis direction as a free standing one dimensional semiconducting nanowire. As seen from the results above, it is known that the absorption is strong when E-field

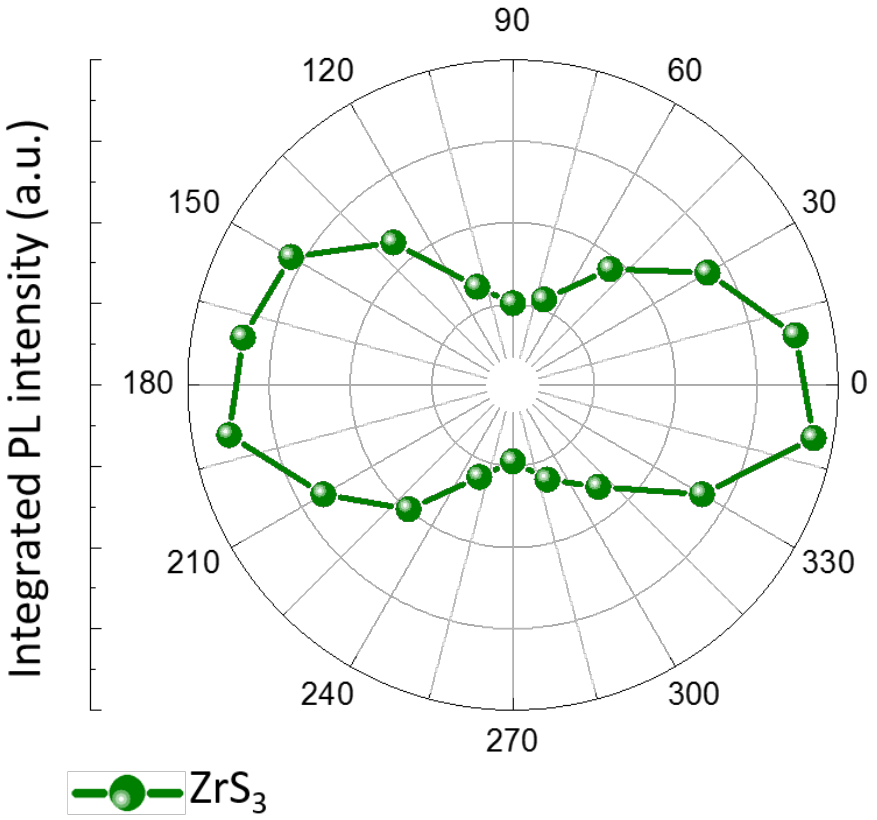

Figure 21. Polar plot of integrated area versus azimuthal flake angle for angle resolved PL in normal configuration.

of the incident polarized laser is aligned along the b-axis direction (E || b). In this case, since the wavelength of light is much smaller than the length of the chain, the electric field induced inside the flake is not significantly reduced. Hence we can say that $E_{in||} = E_{out||}$.

However, when the E-field of the polarized laser is aligned perpendicular to the b-axis direction ($E_{out\perp}$), the wavelength of the exciting light is much larger than the width of an individual chain. Due to this the induced electric field inside the flake ($E_{in\perp}$) is greatly attenuated. If the permittivity contrast between the nanowire and its surrounding medium is $\epsilon(\omega)$, this attenuation can be given by considering the

Figure 22. Left - Free standing 1D ZrS_3 chain. Right - 1D chains embedded in the matrix of ZrS_3

quasi-static case for a cylindrical nanowire. Where ($E_{in\perp}$) is equal to the depolarization factor multiplied by ($E_{out\perp}$) [80]. the ($E_{in\perp}$) can thus be written as:

$$E_{in\perp} = \frac{2.E_{out\perp}}{1 + \epsilon(\omega)} \tag{3.3}$$

Polarization anisotropy (ρ) is then defined as:

$$\rho = \frac{|E_{in||}|^2}{|E_{in\perp}|^2} = \frac{I_{||}}{I_{\perp}} = \frac{|1 + \epsilon(\omega)|^2}{4} \tag{3.4}$$

$I_{||}$ and $I_{\perp}$, or integrated PL intensities were calculated by integrating the PL peak area. The polarization anisotropy (ρ) varied from flake to flake, and varied significantly from orthogonal to normal measurements on the same flake - probably due to the directional selectivity of the detector. Among the data captured for several flakes, the (ρ) varied from 5.7 to 10.8. This suggests that the light emission characteristics from this material can be modulated by up to an order of magnitude by changing the excitation direction.

The (ρ) obtained from ZrS_3 however was still much smaller than that is usually observed among nanowires - (ρ) = 20 - 30. This difference in the polarization anisotropy of ZrS_3 when compared with that of typical nanowires can partly be

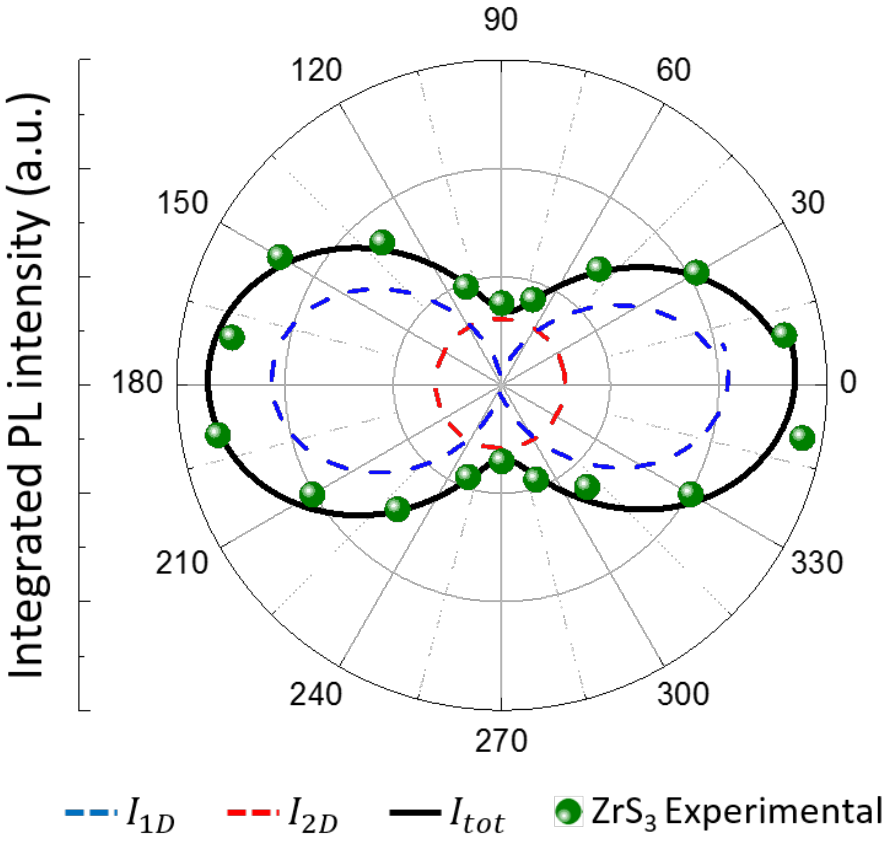

Figure 23. Cosine square fit for I_{1D} and residual I_{2D} contribution for the experimental data.

justified by referring back to the fact that the individual ZrS_6 chains are not free standing in vacuum. In the case of a finitely wide ZrS_3 flake in the a-axis direction, the permittivity contrast ($\epsilon(\omega)_{chain}$) ends up being significantly lower than $\epsilon(\omega)$ as we refer to the 1D chain embedded in a matrix of ZrS_3. This has been represented in the figure 22.

Indeed, a similar reduction in ρ has been observed when luminescent nanowires (ZnO, InP) were coated with Ta_2O_5 [79], surrounded by a matched dielectric medium which was different from vacuum. From materials perspective, this reduction in

polarization anisotropy can be explained when the interaction between quasi-1D chains are accounted for. A closer look at Figure 23 shows that there is still finite amount of PL intensity at 90^o, even when E-field of the incident polarized laser is polarized along the perpendicular direction to the chain direction. In this case, we would expect the the luminescence to be negligible. However, since 1D chains interact with each other, unlike free-standing semiconducting nanowires in vacuum, their optical response can be considered to have two components. One, coming from the 2D-like behaviour, an isotropic optical response, and two, from the 1D nanowire-like anisotropic component. Owing to the only significant component of the E-field (in the direction of b-axis), chain-like PL intensity (I_{1D}) scales as cos^2 which is essentially the same as that for 1D nanowires.

To fit the 1D component of the data into a purely cos^2 function, a following fitting equation is designed (where $A, n, x and B_1$ are fitting parameters):

$$I_{1D} = A.cos^2[(n.\phi) + x] + B_1 \tag{3.5}$$

In the figure 23 this I_{1D} is represented by a dashed blue line. Similar to the constant PL intensity from MoS_2 as seen in figure 20, the constant component (I_{2D} - 2D-like behaviour) of the total luminescence intensity is denoted using a red dashed line in figure 23. The total intensity (I_{tot} shown in a solid black line) is a sum of both intensities from 1D like behaviour (I_{1D}) and intensity from 2D like behaviour (I_{2D}).

Chapter 4

TITANIUM TRISULPHIDE - TiS_3

4.1 Crystal Structure

Isomorphous to ZrS_3, Titanium Trisulphide (TiS_3) crystalizes in a typical monoclinic cell too, with α, $\gamma = 90^o$ and $\beta \neq 90^o$. To visualize the structure, images of several lattices (2 in the a direction, 5 in the b direction and 1 in the c direction) have been shown in the figure 24 a, b and c as seen from axes a [100], b [010] and c [001] respectively. The figure 24 d, represents 2 layers (lattice boundary extended to 2) of TiS_3 stacked and coupled via the van-der-Waals forces. The blue spheres

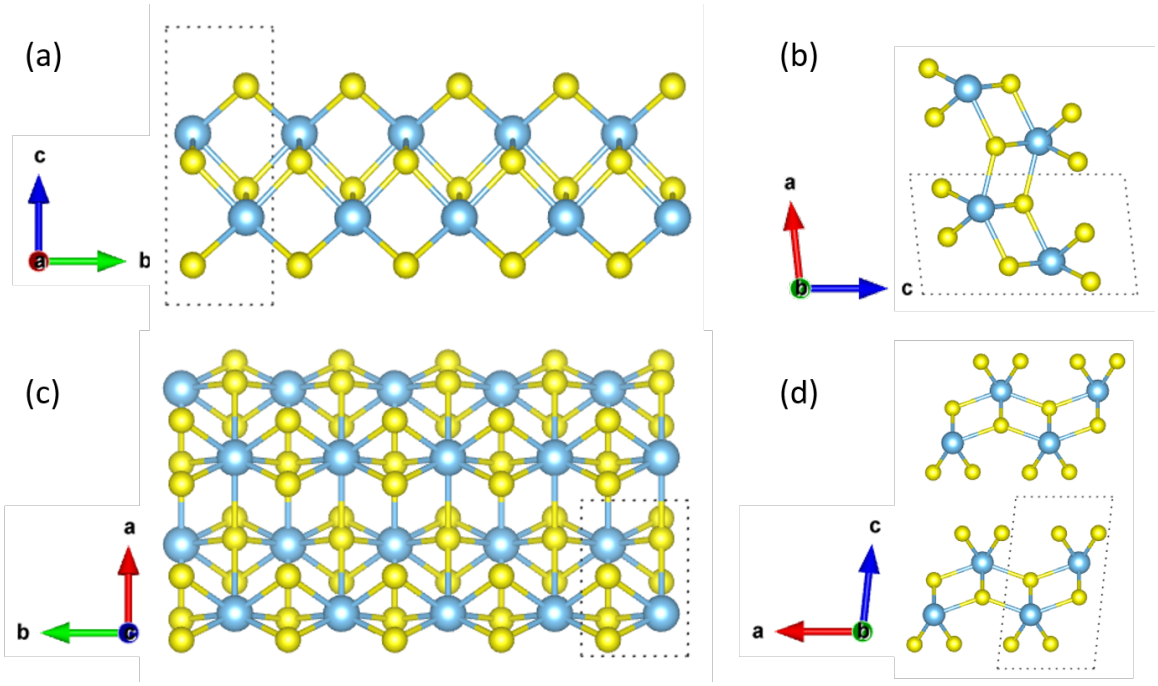

Figure 24. Crystal structure of TiS_3.

represent the Titanium atom and the yellow ones represent the Sulphur atoms. While the dotted black lines show the primitive lattice.

Similar to ZrS_3, the crystal structure of TiS_3 also consists of an array of triangular prisms sharing their triangular faces. The Ti-S bond length between the Ti atom and S atom located in the trigonal prism chain is 2.455 Å, while Ti-S bond length between the Ti atom inside the trigonal prism and S atom of the adjacent chain is 2.648 Å. This suggests that the the prismatic chains are relatively weakly bonded to each other.

In the c-axis direction, as shown in the figure 24d, the layers are stacked and coupled via van-der-Waals forces. This is a relatively weaker coupling than intralayer bonding and makes it easy for TiS_3 to be exfoliated into ultra-thin and monolayers using scotch tape method.

The in-plane anisotropy is also reflected in the grown and exfoliated crystal shapes. The crystals are almost always rectangular in shape where the crystal is elongated in the b-axis direction, or the along chain. During exfoliation of these crystals onto SiO_2/Si and sapphire substrates flakes were consistently seen to be having a high aspect ratio (b-axis : a-axis).

4.2 Growth

TiS_3 whiskers were grown using the Chemical vapor transport (CVT) method wherein the constituent elements were mixed in a stoichiometric ratio and sealed into a quartz tube, and consequently transported to the other end of the tube using a thermal gradient.

Whiskers of TiS_3 were obtained at the cooler end of the tube when 500 mg of Ti

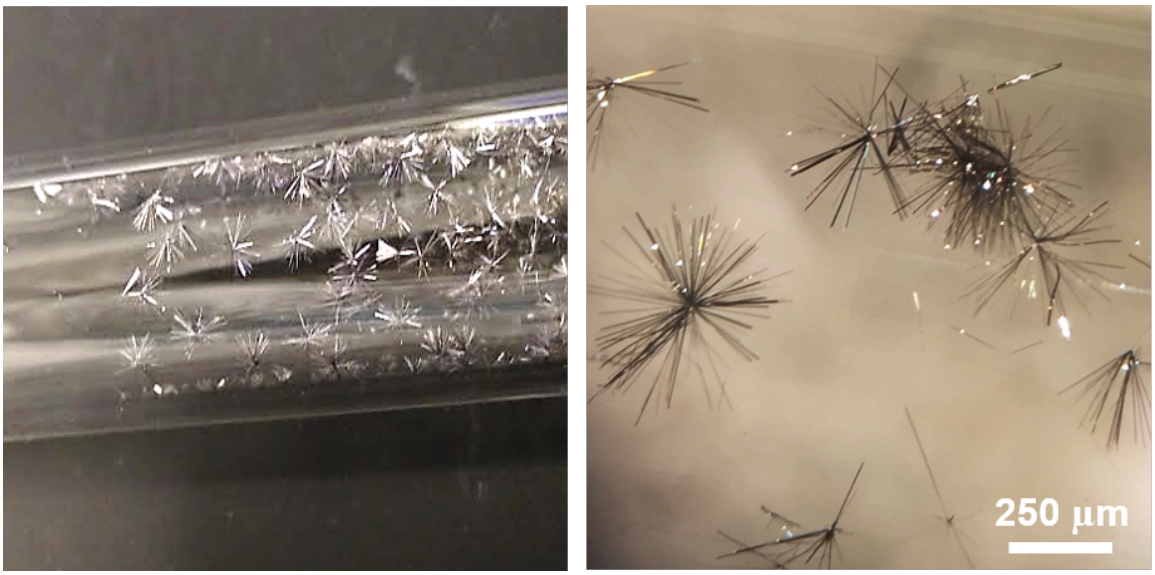

Figure 25. Image of as grown crystal on the inner walls of the sealed tube, macro image (Left to right)

and S were sealed in the tube of diameter 10 mm and length 150 mm, with a molar ratio of 1:3. A Thermo Scientific Lindberg Blue M Tube Furnace with three zones with the tube spanning just two of the zones was used for the growth. The end of the tube containing precursor elements was maintained at 500 ^{o}C, and the other end of the tube was maintained at 80 ^{o}C lower than the hot end. For safety reasons, the temperature was ramped from room temperature to the growth temperature in 24 hours. The growth temperature was maintained for four days and then the furnace was let to cool naturally.

The crystals obtained as a result of this growth were highly elongated and thin whiskers growing outward from a nucleation point as seen in figure 25, resembling a flower. On an average, each whisker measured from 250 - 500 μm

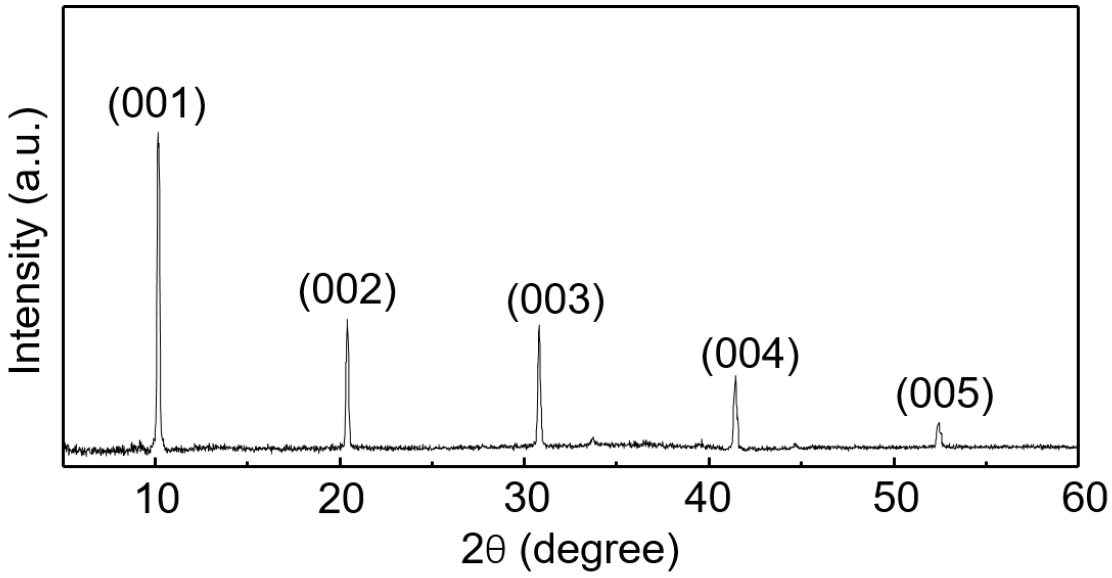

Figure 26. Powder XRD data of TiS_3 whiskers.

4.3 XRD Data

The X-ray diffraction (XRD) patterns were recorded using a Siemens D5000 powder diffractometer with CuKα radiation ($\lambda = 1.54$ Å). It is to be noted that the mounted crystals were fairly flat on the plane perpendicular to the c-axis. Thus with their placement on the sample holder, they naturally arranged themselves with c-axis facing upwards. It is evident from the XRD data that only the planes perpendicular to c-axis were clearly shown. Although this is not a complete spectra, it is sufficient to verify the phase of the material.

A few crystals were first arranged on the zero-background plate, so as to maximise the x-ray exposure and the measurement was done for $2\theta = 5$ to 60 degrees. The XRD pattern obtained was found to be consistent with ICDD 15-0783. Intense peaks also suggest that the material was well crystallized during the growth. The same equations that were used to confirm the peaks missing from the database.

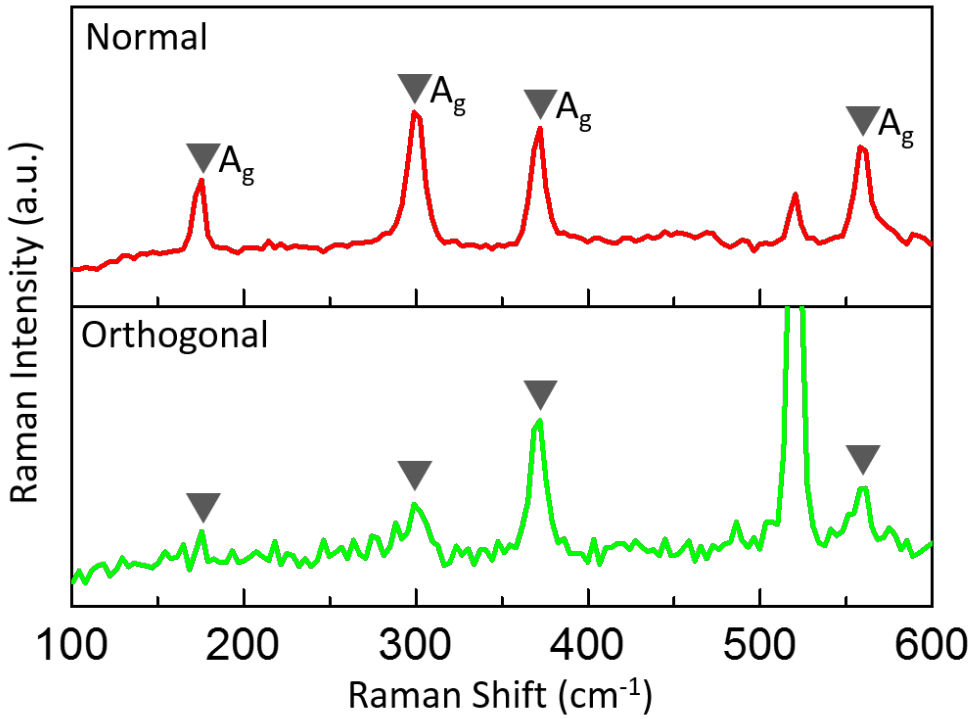

Figure 27. Raman spectra of exfoliated TiS_3 whiskers.

XRD data and the corresponding matched card confirm that the the material got crystallized in a monoclinic cell with the following lattie parameters: a = 4.973 Å, b = 3.433 Å, c = 8.714 Å, and $\beta = 97.74^o$. The FWHM of peaks were not used to determine the crystallite size as the crystals were far too larger than recommended for this approximation.

4.4 Raman Spectra

TiS_3 is isomorphous with ZrS_3, so the mechanical representations of the vibration modes are same as that of ZrS_3, 3 acoustic and 21 optical modes in the first brillouin

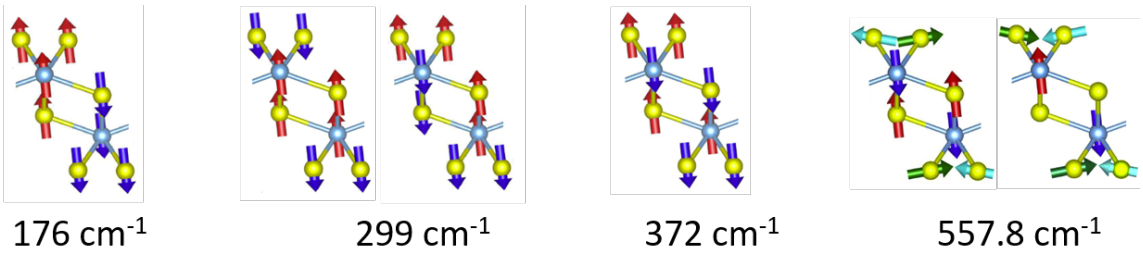

Figure 28. Raman active optical modes in TiS_3 corresponding to their mentioned frequencies.

zone. Raman was measured using a 488 nm laser on crystals exfoliated onto 290 nm SiO_2/Si substrate. Consistent with previous reports [81], peaks were observed at 175.5 cm^{-1}, 299 cm^{-1}, 372 cm^{-1} and 557.8 cm^{-1}. The peak at 520 cm^{-1} originates from the Silicon substrate, which does not interfere with any peaks and at the same time serves as a good standard to compare the relative intensities of the peaks from TiS_3.

In the normal configuration, where the E-field of the incident polarized laser was polarized along the b-axis, peaks observed were fairly intense. Strong raman peaks corroborate XRD data and suggest good crystallinity. Hoever, weak intensities of all the peaks in the orthogonal configuration suggest that the peaks are of A_g nature. This can be said because according to the Loudon's [74] polarisability tensors, only if a peak appears intense in cross polarizations, it can be labled as B_g.

To understand the fundamental origin of the individual peaks, finite displacement calculations were performed (shown in figure 28). The displacement calculations show the origin of each peak in the Raman spectra.

The lowest frequency peak at 175.5 cm^{-1} has been found to originate from an out-of-phase rigid vibrations of individual chains in the unit cell. The vibration happens in the out-of-plane (c-axis) direction and retains the rigidity of the chain as the Zr-S bond modulation is not involved. Thus, it has been labeled as the A_g^{rigid}. It

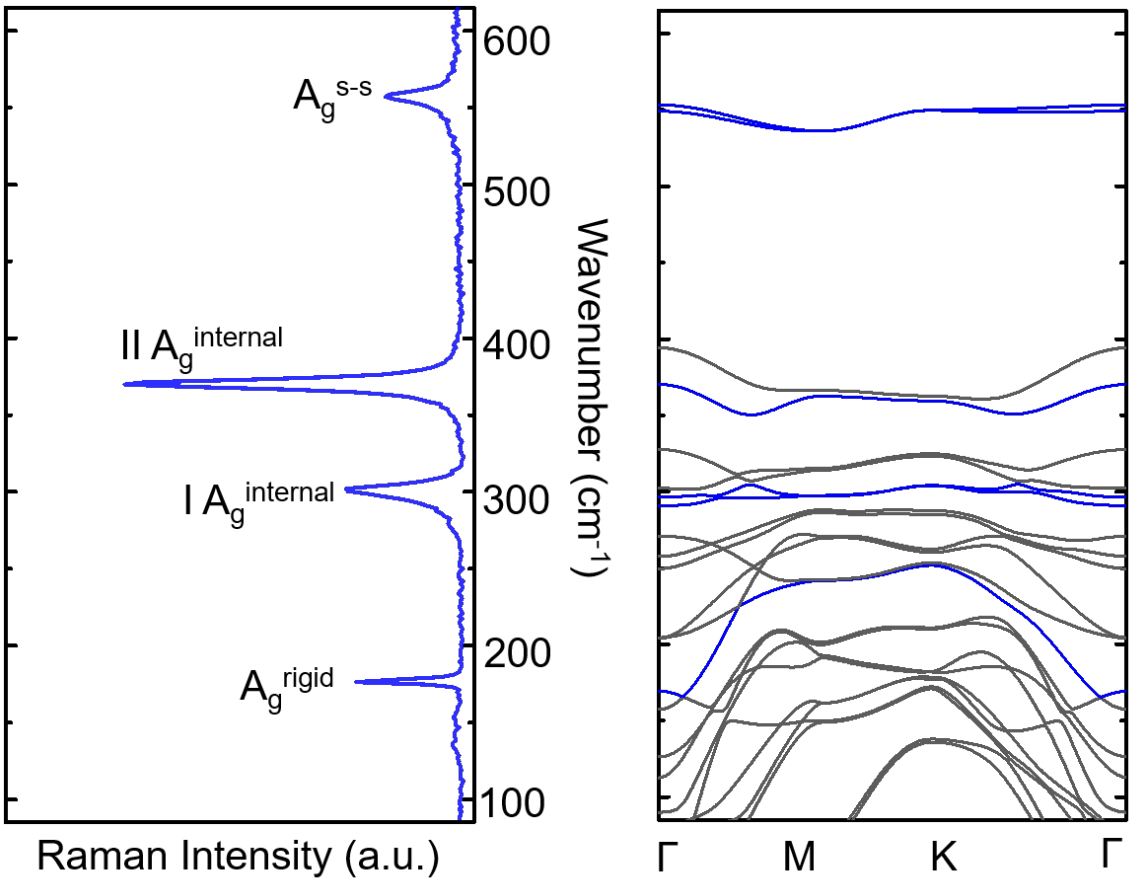

Figure 29. Corresponding raman spectrum and phonon dispersion spectrum calculated from first principle density function theory (DFT) for TiS3.

can be visualized as 2 elongated chains rigidly moving with respect to each other (as shown in figure 28 while not affecting the Zr-S bond distance.

Unlike the lowest frequency mode, the 299 cm^{-1} and 372 cm^{-1} mode involve internal vibrations too. Due to the involvement of internal vibrations within the TiS_3 layers, these modes have been labeled as I $A_g^{internal}$ and II $A_g^{internal}$ respectively. A closer look into the 299 cm^{-1} reveals two degenerate optical branches in the phonon dispersion which almost coincide at the Γ point. The basic thing that differentiates one of this mode from other is the relative vibration direction between the Ti, S atoms,

and S-S pairs across the two prisms. Due to the presence of two closely spaced modes and due to the resolution limit of the equipment, a single peak appears. However, the FWHM of this peak is significantly wider than the other peaks with no degeneracy at 12 cm^{-1}.

The peak at 557.8 cm^{-1}, or the highest frequency peak also appears to be a degenerate peak as the DFT calculation of phonon dispersion (figure 29) shows two very closely spaced optical branches (top-most branches). These modes consist of in-plane out-of-phase motion of S-S pair and out-of-plane motion of Ti and the S atoms as represented in figure 28. Again, owing to the peak parenting two degenerate modes, it also appears with a higher FWHM than the other non-degenerate peaks 12 cm^{-1}. Due to its signature vibration involving the S-S pair, this peak is labeled as A_g^{S-S}

4.5 Angle Dependent Raman

The angle dependent Raman was measured for flakes exfoliated on 290 nm SiO_2/Si substrate for both orthogonal and normal arrangements. Raman spectra was recorded for a flake angle ranging from 0 to 360 degrees with a step size of 10 degrees. The resultant 3D plot in orthogonal and normal geometries have been shown in figure 30 and 31, respectively.

It is observed that both the plots show a 180 degree periodicity. However the periodicity is very different from what is observed in ZrS_3. In orthogonal arrangement, as expected, the intensity reaches a maximum at 90 and 270 degrees. But at the angles, 0 and 180 degrees, where a minimum is expected, the plot reaches an intermediate

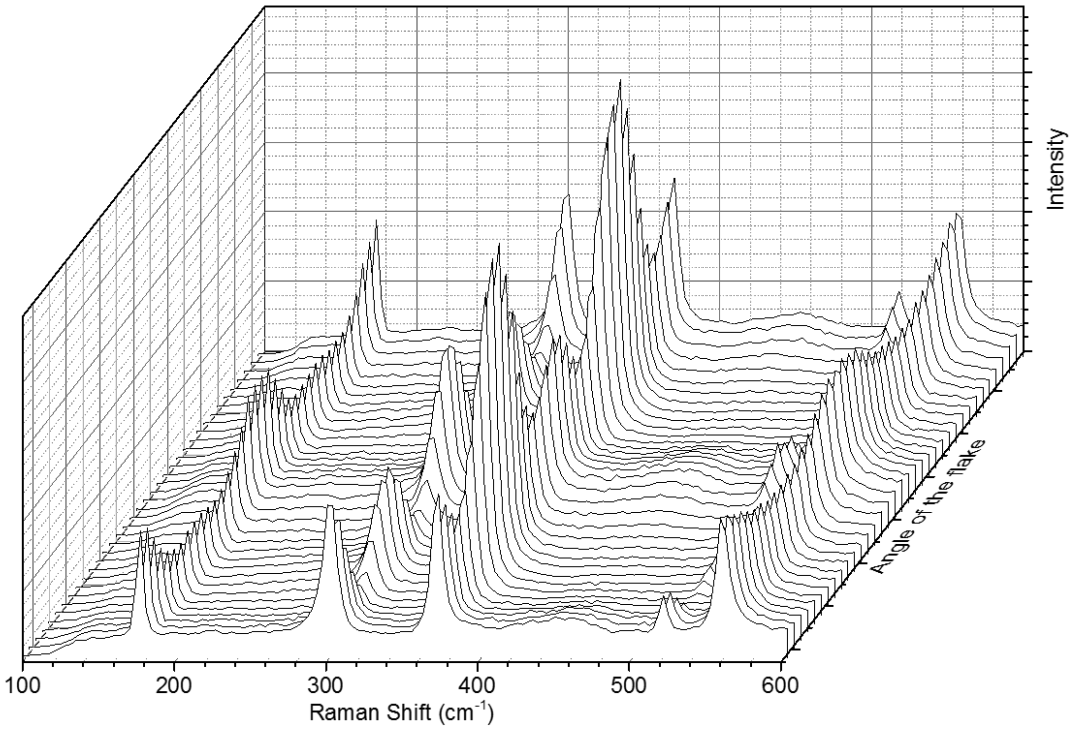

Figure 30. 3D angle dependent Raman plot in orthogonal arrangement for TiS_3

local maxima which is significantly lower in intensity than the global maxima. This four lobed feature of $A_g^{internal}$ and A_g^{rigid} peaks, can be clearly visualized with the help of a polar plot where the angle dependent intensity these peaks in orthogonal arrangement is shown in figure 32 (left). Unlike the 372 cm^{-}1 peak, the two lowest frequency peaks appear 90 degree phase shifted, with global maximums appearing at 0 and 180 degrees. Interestingly, the A_g^{S-S} stands out, showing an elliptical (no lobes) behaviour, with global maximums at 0 and 180 degrees. This is interesting because, even the silicon peak shows a four lobed feature in all the experiments (seen in figure 31).

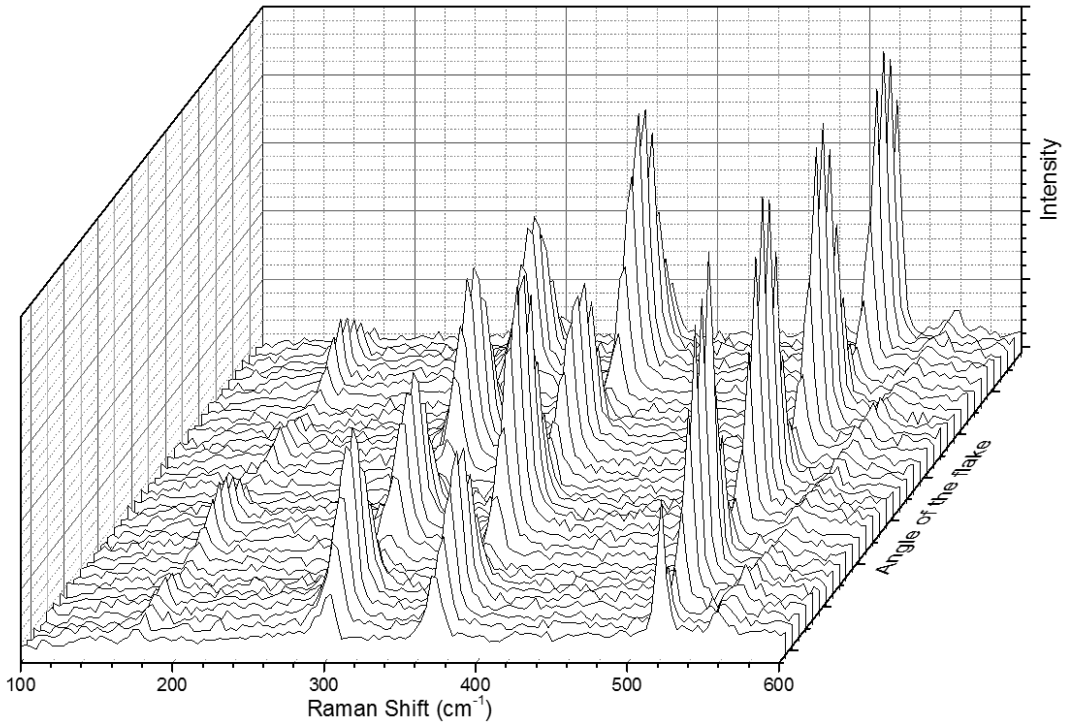

Figure 31. 3D angle dependent Raman plot in normal arrangement for TiS_3

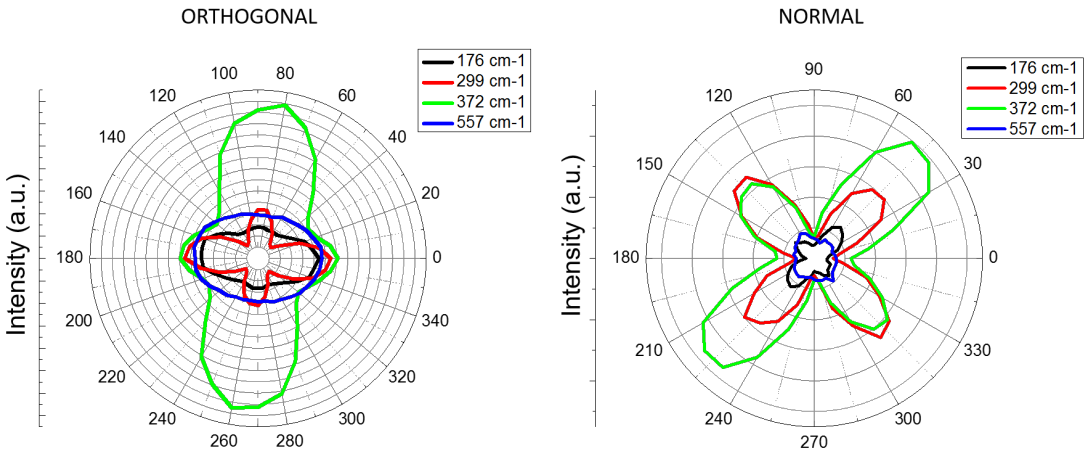

Figure 32. Polar plots for intensity versus angle for TiS_3 in orthogonal (left) and Normal (right) arrangments

Similarly, in normal arrangement (shown in figure 32 - right) a similar behaviour with a 45 degree phase shift can be observed for all the peaks. The maximums appear at 45, 135, 225 and 315 degrees, while the minimums occur at 0, 90, 180 and 360 degrees. Although a clear trend can be seen with most peaks, the A_g^{S-S} peak falls in the noise range and a does not show a clear trend in normal arrangement.

Since the lack of ability of available instruments to characterize the PL properties of micro TiS_3 whiskers (which have an anticipated optical band gap in the infrared region), these experiments were not conducted as a part of this thesis.

Chapter 5

CONCLUSION AND FUTURE PROSPECTS

5.1 Introduction

Two dimensional layered materials (2DLMs), such as Graphene, h-BN and Transition Metal Dichalcogenides, has been an intensely active area of research owing to their stellar physical properties which have allowed observations of novel physics and proof-of-concept nano-electronic devices with performances previously never seen with traditional semiconductors. With the constant reduction of sizes of electronic devices and the advent of flexible and wearable technologies expects devices to perform a variety of functions. Thus the future of electronics beckons for a family of stable 2DLMs with varying physical properties that allow these range of functions.

Currently, the family of available layered materials indeed has grown to include materials that allow devices to be fabricated with a range of functions. However, most of these materials consist of layers that has atoms held together with covalent forces which are isotropic in nature, in both the in-plane crystalline directions. This leads to materials with isotropic in-plane properties and allows little room (undesirably complicated devices) for devices that desire polarization dependent functionality. A few popular 2DLMs currently touted to posses in-plane anisotropy are either not stable in the air (Phosphorene) or show mildly anisotropic properties in thick flake regimes (Group V TMDCs, like ReS_2 and $ReSe_2$).

There exist a family of layered materials of the form MX_3 (M = IVB or VB group elements and X = S, Se or Te). Resembling other known layered compounds such

as TMDCs, MX_3 compounds exhibit an analogous layered structure with individual layers coupled by van-der-Waals forces. However, their in-plane anisotropic crystalline and physical properties makes them stand out from the conventional layered materials. MX_3 compounds owe this anisotropic behavior to their structurally anisotropic crystal structure consisting of infinite one-dimensional MX6 trigonal prism unit chains which bond relatively weakly to other such parallel running chains, and form a slab (layer) of material with significantly different properties parallel and perpendicular to these chains within the layer. Although MX_3 type crystals have long been known to exhibit anisotropy, in the light of the present-day relevance of aligned nanowires, quasi-2D and 2D materials, we present a report on the atypical optical properties of ZrS_3 & TiS_3, and propose features which it and its analogues can potentially drive fresh opportunities in technologies involving polarized detection, near-field imaging, communication systems, and bio-applications relying on the generation and detection of polarized light.

5.2 Growth and Sample Preperation

The growth of both the crystals (ZrS_3 and TiS_3) were done by CVT technique and crystals of the shape of whiskers were obtained. ZrS_3 and TiS_3 were grown using a two zones furnace, inside vacuum sealed quartz tubes with precursors placed at temperatures 600 and 500 ^oC, respectively. Macro sized elongated crystals obtained were then exfoliated onto SiO_2/Si substrates to carry out further examination using optical techniques such as Raman and PL.

5.3 Material Characterization

Crystal quality and the phase was confirmed by powder XRD. Intense Raman peaks for both the crystals corroborated the good quality of the crystal.

Despite being an indirect bandgap semiconductor with a bandgap of 1.88 eV, ZrS_3 was observed to be luminescent at room temperature. PL peaks were observed at 1.8 and 1.45 eV. The power dependence PL spectra suggests their origin to be from band to band (or delocalized impurity band to band) and from bound excitons respectively.

Angle resolved Pl spectra of ZrS_3 showed a cosine square variation of integrated PL intensity with respect to the azimuthal flake angle when polarized laser was incident perpendicular to the van-der-Waals plane. For polarizations in the direction of the length of chains (b-axis), a maximum PL intensity was reached and a minimum was reached when polarization was perpendicular to the b-axis. A PL polarization anisotropy spanning from 5.7 to 10.8 was observed for various flakes. Probably varying due to differences in defect densities. PL spectra for TiS_3 could not be recorded due to limited detector ability in the raman instrument for IR ranges (as estimated bandgap for TiS_3 lies in the IR range).

Angle dependent raman spectra plotted in the polar plot representing raman intensity in the y-axis vs the angle of the flake for ZrS_3 appeared two-lobed in the orthogonal and four-lobed in the normal arrangement. Orthogonal arrangement showed maxima at 90 and 270 degrees, again, where the polarization was aligned in the chain direction. However maxima at every 90 degree intervals, starting from 45 degrees.

Angle dependent Raman spectra for TiS_3 appeared four lobed in both the arrangements. However, there were only two global maximas. Again maxima in the

orthogonal arrangement occurred when the polarization was aligned in the direction of the chain (at 90 and 270 degrees). In the normal, the polar plot appeared to have rotated by 45 degrees. The S-S vibration mode showed an interesting behaviour with an elliptical polar plot.

5.4 Conclusion

Angle dependent raman and PL measurements confirm the anisotropy of both TiS_3 and ZrS_3 within the van-der-Waals plane, in relatively thick regimes, both of which belong to a new class of anisotropic layered materials of the form MX_3s. Both these materials have been found to be stable in the air for long periods of time. Extent of PL polarization anisotropy observed was close to that of purely 1D behaviour, however due to the 2D like contribution in these quasi-1D materials, it is actually slightly lower than purely 1D materials. Among 2D materials, through these PL intensity variation with angle, ZrS_3 appears to be a potential candidate for applications relying on the generation and detection of polarized light.

5.5 Future Work

1. Future work involving the establishment of these materials could involve angle resolved intrinsic transport measurements. Or angle dependent measurements in devices fabricated using MX_3s, in combination (heterojunctions) with other isotropic or anisotropic 2DLMs.

2. Development of CVT methods to directly obtain p and n type doped bulk crystals, doped with elements such as Ti, Zr or Hf.

3. Intercalation of chemically active species such as Lithium, Bromine, Pyridine etc into these materials could lead to their practical applications in novel devices and integration with existing devices.

4. Bottom-up CVD growth parameter of MX_3 materials can be established for directly obtaining higher quantities of crystals in ultra-thin regimes for industrial level scaling towards wafer scale growth.

REFERENCES

[1] K. Novoselov, D. Jiang, F. Schedin, T. Booth, V. Khotkevich, S. Morozov, and A. Geim, "Two-dimensional atomic crystals," *Proceedings of the National Academy of Sciences of the United States of America*, vol. 102, no. 30, pp. 10451–10453, 2005.

[2] K. Novoselov, A. K. Geim, S. Morozov, D. Jiang, M. Katsnelson, I. Grigorieva, S. Dubonos, and A. Firsov, "Two-dimensional gas of massless dirac fermions in graphene," *nature*, vol. 438, no. 7065, pp. 197–200, 2005.

[3] A. K. Geim and K. S. Novoselov, "The rise of graphene," *Nature materials*, vol. 6, no. 3, pp. 183–191, 2007.

[4] K. F. Mak, C. Lee, J. Hone, J. Shan, and T. F. Heinz, "Atomically thin mos 2: a new direct-gap semiconductor," *Physical Review Letters*, vol. 105, no. 13, p. 136805, 2010.

[5] A. K. Geim and I. V. Grigorieva, "Van der waals heterostructures," *Nature*, vol. 499, no. 7459, pp. 419–425, 2013.

[6] M. Chhowalla, H. S. Shin, G. Eda, L.-J. Li, K. P. Loh, and H. Zhang, "The chemistry of two-dimensional layered transition metal dichalcogenide nanosheets," *Nature chemistry*, vol. 5, no. 4, pp. 263–275, 2013.

[7] G. S. Duesberg, "Heterojunctions in 2d semiconductors: A perfect match," *Nature materials*, vol. 13, no. 12, pp. 1075–1076, 2014.

[8] Q. H. Wang, K. Kalantar-Zadeh, A. Kis, J. N. Coleman, and M. S. Strano, "Electronics and optoelectronics of two-dimensional transition metal dichalcogenides," *Nature nanotechnology*, vol. 7, no. 11, pp. 699–712, 2012.

[9] C. Lee, X. Wei, J. W. Kysar, and J. Hone, "Measurement of the elastic properties and intrinsic strength of monolayer graphene," *science*, vol. 321, no. 5887, pp. 385–388, 2008.

[10] F. Schwierz, "Graphene transistors," *Nature nanotechnology*, vol. 5, no. 7, pp. 487–496, 2010.

[11] S. Bae, H. Kim, Y. Lee, X. Xu, J.-S. Park, Y. Zheng, J. Balakrishnan, T. Lei, H. R. Kim, Y. I. Song, *et al.*, "Roll-to-roll production of 30-inch graphene films for transparent electrodes," *Nature nanotechnology*, vol. 5, no. 8, pp. 574–578, 2010.

[12] K. F. Mak, M. Y. Sfeir, Y. Wu, C. H. Lui, J. A. Misewich, and T. F. Heinz, "Measurement of the optical conductivity of graphene," *Physical review letters*, vol. 101, no. 19, p. 196405, 2008.

[13] X. Wang, L. Zhi, and K. Müllen, "Transparent, conductive graphene electrodes for dye-sensitized solar cells," *Nano letters*, vol. 8, no. 1, pp. 323–327, 2008.

[14] Y. U. Jung, K.-W. Park, S.-T. Hur, S.-W. Choi, and S. J. Kang, "High-transmittance liquid-crystal displays using graphene conducting layers," *Liquid Crystals*, vol. 41, no. 1, pp. 101–105, 2014.

[15] L. Song, L. Ci, H. Lu, P. B. Sorokin, C. Jin, J. Ni, A. G. Kvashnin, D. G. Kvashnin, J. Lou, B. I. Yakobson, *et al.*, "Large scale growth and characterization of atomic hexagonal boron nitride layers," *Nano letters*, vol. 10, no. 8, pp. 3209–3215, 2010.

[16] K. Watanabe, T. Taniguchi, and H. Kanda, "Direct-bandgap properties and evidence for ultraviolet lasing of hexagonal boron nitride single crystal," *Nature materials*, vol. 3, no. 6, pp. 404–409, 2004.

[17] Y. Kubota, K. Watanabe, O. Tsuda, and T. Taniguchi, "Deep ultraviolet light-emitting hexagonal boron nitride synthesized at atmospheric pressure," *Science*, vol. 317, no. 5840, pp. 932–934, 2007.

[18] R. A. Doganov, E. C. O'Farrell, S. P. Koenig, Y. Yeo, A. Ziletti, A. Carvalho, D. K. Campbell, D. F. Coker, K. Watanabe, T. Taniguchi, *et al.*, "Transport properties of pristine few-layer black phosphorus by van der waals passivation in an inert atmosphere," *Nature communications*, vol. 6, 2015.

[19] C. R. Dean, A. F. Young, I. Meric, C. Lee, L. Wang, S. Sorgenfrei, K. Watanabe, T. Taniguchi, P. Kim, K. Shepard, *et al.*, "Boron nitride substrates for high-quality graphene electronics," *Nature nanotechnology*, vol. 5, no. 10, pp. 722–726, 2010.

[20] J. H. Warner, M. H. Rummeli, A. Bachmatiuk, and B. Buchner, "Atomic resolution imaging and topography of boron nitride sheets produced by chemical exfoliation," *ACS nano*, vol. 4, no. 3, pp. 1299–1304, 2010.

[21] X. Li, W. Cai, J. An, S. Kim, J. Nah, D. Yang, R. Piner, A. Velamakanni, I. Jung, E. Tutuc, *et al.*, "Large-area synthesis of high-quality and uniform graphene films on copper foils," *Science*, vol. 324, no. 5932, pp. 1312–1314, 2009.

[22] W. Gannett, W. Regan, K. Watanabe, T. Taniguchi, M. Crommie, and A. Zettl, "Boron nitride substrates for high mobility chemical vapor deposited graphene," *Applied Physics Letters*, vol. 98, no. 24, p. 242105, 2011.

[23] Z. H. Ni, T. Yu, Y. H. Lu, Y. Y. Wang, Y. P. Feng, and Z. X. Shen, "Uniaxial strain on graphene: Raman spectroscopy study and band-gap opening," *ACS nano*, vol. 2, no. 11, pp. 2301–2305, 2008.

[24] V. M. Pereira, A. C. Neto, and N. Peres, "Tight-binding approach to uniaxial strain in graphene," *Physical Review B*, vol. 80, no. 4, p. 045401, 2009.

[25] S. Zhou, G.-H. Gweon, A. Fedorov, P. First, W. De Heer, D.-H. Lee, F. Guinea, A. C. Neto, and A. Lanzara, "Substrate-induced bandgap opening in epitaxial graphene," *Nature materials*, vol. 6, no. 10, pp. 770–775, 2007.

[26] Y. Zhang, T.-T. Tang, C. Girit, Z. Hao, M. C. Martin, A. Zettl, M. F. Crommie, Y. R. Shen, and F. Wang, "Direct observation of a widely tunable bandgap in bilayer graphene," *Nature*, vol. 459, no. 7248, pp. 820–823, 2009.

[27] E. McCann, "Asymmetry gap in the electronic band structure of bilayer graphene," *Physical Review B*, vol. 74, no. 16, p. 161403, 2006.

[28] X. Duan, C. Wang, A. Pan, R. Yu, and X. Duan, "Two-dimensional transition metal dichalcogenides as atomically thin semiconductors: opportunities and challenges," *Chemical Society Reviews*, vol. 44, no. 24, pp. 8859–8876, 2015.

[29] H.-P. Komsa, J. Kotakoski, S. Kurasch, O. Lehtinen, U. Kaiser, and A. V. Krasheninnikov, "Two-dimensional transition metal dichalcogenides under electron irradiation: defect production and doping," *Physical review letters*, vol. 109, no. 3, p. 035503, 2012.

[30] C. Tan and H. Zhang, "Two-dimensional transition metal dichalcogenide nanosheet-based composites," *Chemical Society Reviews*, vol. 44, no. 9, pp. 2713–2731, 2015.

[31] W. S. Yun, S. Han, S. C. Hong, I. G. Kim, and J. Lee, "Thickness and strain effects on electronic structures of transition metal dichalcogenides: 2h-m x 2 semiconductors (m= mo, w; x= s, se, te)," *Physical Review B*, vol. 85, no. 3, p. 033305, 2012.

[32] C. Mai, A. Barrette, Y. Yu, Y. G. Semenov, K. W. Kim, L. Cao, and K. Gundogdu, "Many-body effects in valleytronics: Direct measurement of valley lifetimes in single-layer mos2," *Nano letters*, vol. 14, no. 1, pp. 202–206, 2013.

[33] H.-M. Li, D.-Y. Lee, M. S. Choi, D. Qu, X. Liu, C.-H. Ra, and W. J. Yoo, "Metal-semiconductor barrier modulation for high photoresponse in transition metal dichalcogenide field effect transistors," *Scientific reports*, vol. 4, 2014.

[34] A. Nourbakhsh, A. Zubair, M. S. Dresselhaus, and T. Palacios, "Transport properties of a mos2/wse2 heterojunction transistor and its potential for application," *Nano letters*, 2016.

[35] N. Flöry, A. Jain, P. Bharadwaj, M. Parzefall, T. Taniguchi, K. Watanabe, and L. Novotny, "A wse2/mose2 heterostructure photovoltaic device," *Applied Physics Letters*, vol. 107, no. 12, p. 123106, 2015.

[36] S. Wi, M. Chen, H. Nam, A. C. Liu, E. Meyhofer, and X. Liang, "High blue-near ultraviolet photodiode response of vertically stacked graphene-mos2-metal heterostructures," *Applied Physics Letters*, vol. 104, no. 23, p. 232103, 2014.

[37] M.-L. Tsai, S.-H. Su, J.-K. Chang, D.-S. Tsai, C.-H. Chen, C.-I. Wu, L.-J. Li, L.-J. Chen, and J.-H. He, "Monolayer mos2 heterojunction solar cells," *Acs Nano*, vol. 8, no. 8, pp. 8317–8322, 2014.

[38] K.-A. N. Duerloo, M. T. Ong, and E. J. Reed, "Intrinsic piezoelectricity in two-dimensional materials," *The Journal of Physical Chemistry Letters*, vol. 3, no. 19, pp. 2871–2876, 2012.

[39] A. Neto and K. Novoselov, "Two-dimensional crystals: beyond graphene," *Materials Express*, vol. 1, no. 1, pp. 10–17, 2011.

[40] S. Z. Butler, S. M. Hollen, L. Cao, Y. Cui, J. A. Gupta, H. R. Gutiérrez, T. F. Heinz, S. S. Hong, J. Huang, A. F. Ismach, *et al.*, "Progress, challenges, and opportunities in two-dimensional materials beyond graphene," *ACS nano*, vol. 7, no. 4, pp. 2898–2926, 2013.

[41] P. Vogt, P. De Padova, C. Quaresima, J. Avila, E. Frantzeskakis, M. C. Asensio, A. Resta, B. Ealet, and G. Le Lay, "Silicene: compelling experimental evidence for graphenelike two-dimensional silicon," *Physical review letters*, vol. 108, no. 15, p. 155501, 2012.

[42] A. J. Mannix, X.-F. Zhou, B. Kiraly, J. D. Wood, D. Alducin, B. D. Myers, X. Liu, B. L. Fisher, U. Santiago, J. R. Guest, *et al.*, "Synthesis of borophenes: Anisotropic, two-dimensional boron polymorphs," *Science*, vol. 350, no. 6267, pp. 1513–1516, 2015.

[43] E. S. Reich *et al.*, "Phosphorene excites materials scientists," *Nature*, vol. 506, no. 7486, p. 19, 2014.

[44] M. Dávila, L. Xian, S. Cahangirov, A. Rubio, and G. Le Lay, "Germanene: a novel two-dimensional germanium allotrope akin to graphene and silicene," *New Journal of Physics*, vol. 16, no. 9, p. 095002, 2014.

[45] P. Tang, P. Chen, W. Cao, H. Huang, S. Cahangirov, L. Xian, Y. Xu, S.-C. Zhang, W. Duan, and A. Rubio, "Stable two-dimensional dumbbell stanene: A quantum spin hall insulator," *Physical Review B*, vol. 90, no. 12, p. 121408, 2014.

[46] A. Molle, C. Grazianetti, D. Chiappe, E. Cinquanta, E. Cianci, G. Tallarida, and M. Fanciulli, "Hindering the oxidation of silicene with non-reactive encapsulation," *Advanced Functional Materials*, vol. 23, no. 35, pp. 4340–4344, 2013.

[47] D. J. Late, B. Liu, H. Matte, C. Rao, and V. P. Dravid, "Rapid characterization of ultrathin layers of chalcogenides on sio2/si substrates," *Advanced Functional Materials*, vol. 22, no. 9, pp. 1894–1905, 2012.

[48] Y. Ma, Y. Dai, M. Guo, L. Yu, and B. Huang, "Tunable electronic and dielectric behavior of gas and gase monolayers," *Physical Chemistry Chemical Physics*, vol. 15, no. 19, pp. 7098–7105, 2013.

[49] S. Lei, L. Ge, S. Najmaei, A. George, R. Kappera, J. Lou, M. Chhowalla, H. Yamaguchi, G. Gupta, R. Vajtai, *et al.*, "Evolution of the electronic band structure and efficient photo-detection in atomic layers of inse," *ACS nano*, vol. 8, no. 2, pp. 1263–1272, 2014.

[50] J. Zhang, T. Song, Z. Zhang, K. Ding, F. Huang, and B. Sun, "Layered ultrathin pbi 2 single crystals for high sensitivity flexible photodetectors," *Journal of Materials Chemistry C*, vol. 3, no. 17, pp. 4402–4406, 2015.

[51] H. Liu, A. T. Neal, Z. Zhu, Z. Luo, X. Xu, D. Tománek, and P. D. Ye, "Phosphorene: an unexplored 2d semiconductor with a high hole mobility," *ACS nano*, vol. 8, no. 4, pp. 4033–4041, 2014.

[52] K. Friemelt, M.-C. Lux-Steiner, and E. Bucher, "Optical properties of the layered transition-metal-dichalcogenide res2: Anisotropy in the van der waals plane," *Journal of applied physics*, vol. 74, no. 8, pp. 5266–5268, 1993.

[53] A. Grisel, F. Levy, and T. Wieting, "Optical-phonon anisotropies in crystalline ivb trichalcogenides," *Physica B+ C*, vol. 99, no. 1, pp. 365–370, 1980.

[54] H. Zhao, J. Wu, H. Zhong, Q. Guo, X. Wang, F. Xia, L. Yang, P. Tan, and H. Wang, "Interlayer interactions in anisotropic atomically thin rhenium diselenide," *Nano Research*, vol. 8, no. 11, pp. 3651–3661, 2015.

[55] S. Tongay, H. Sahin, C. Ko, A. Luce, W. Fan, K. Liu, J. Zhou, Y.-S. Huang, C.-H. Ho, J. Yan, *et al.*, "Monolayer behaviour in bulk res2 due to electronic and vibrational decoupling," *Nature communications*, vol. 5, 2014.

[56] J. Wilson and A. Yoffe, "The transition metal dichalcogenides discussion and interpretation of the observed optical, electrical and structural properties," *Advances in Physics*, vol. 18, no. 73, pp. 193–335, 1969.

[57] C. Ho, Y. Huang, K. Tiong, and P. Liao, "In-plane anisotropy of the optical and electrical properties of layered res2 crystals," *Journal of Physics: Condensed Matter*, vol. 11, no. 27, p. 5367, 1999.

[58] E. Liu, Y. Fu, Y. Wang, Y. Feng, H. Liu, X. Wan, W. Zhou, B. Wang, L. Shao, C.-H. Ho, *et al.*, "Integrated digital inverters based on two-dimensional anisotropic res2 field-effect transistors," *Nature communications*, vol. 6, 2015.

[59] D. A. Chenet, O. B. Aslan, P. Y. Huang, C. Fan, A. M. van der Zande, T. F. Heinz, and J. C. Hone, "In-plane anisotropy in mono-and few-layer res2 probed by raman spectroscopy and scanning transmission electron microscopy," *Nano letters*, vol. 15, no. 9, pp. 5667–5672, 2015.

[60] D. Wolverson, S. Crampin, A. S. Kazemi, A. Ilie, and S. J. Bending, "Raman spectra of monolayer, few-layer, and bulk rese2: An anisotropic layered semiconductor," *ACS nano*, vol. 8, no. 11, pp. 11154–11164, 2014.

[61] Y.-C. Lin, H.-P. Komsa, C.-H. Yeh, T. Bjorkman, Z.-Y. Liang, C.-H. Ho, Y.-S. Huang, P.-W. Chiu, A. V. Krasheninnikov, and K. Suenaga, "Single-layer res2: Two-dimensional semiconductor with tunable in-plane anisotropy," *ACS nano*, vol. 9, no. 11, pp. 11249–11257, 2015.

[62] V. Tran, R. Soklaski, Y. Liang, and L. Yang, "Layer-controlled band gap and anisotropic excitons in few-layer black phosphorus," *Physical Review B*, vol. 89, no. 23, p. 235319, 2014.

[63] J. Qiao, X. Kong, Z.-X. Hu, F. Yang, and W. Ji, "High-mobility transport anisotropy and linear dichroism in few-layer black phosphorus," *Nature communications*, vol. 5, 2014.

[64] F. Xia, H. Wang, and Y. Jia, "Rediscovering black phosphorus as an anisotropic layered material for optoelectronics and electronics," *Nature communications*, vol. 5, 2014.

[65] R. Fei and L. Yang, "Strain-engineering the anisotropic electrical conductance of few-layer black phosphorus," *Nano letters*, vol. 14, no. 5, pp. 2884–2889, 2014.

[66] S. Jandl, C. D. Cavellin, and J. Harbec, "Raman spectra of zrs 3," *Solid State Communications*, vol. 31, no. 5, pp. 351–353, 1979.

[67] A. Ait-Ouali and S. Jandl, "Two-dimensional indirect excitons in the layer-type trichalcogenide zrs 3," *Physical Review B*, vol. 49, no. 3, p. 1813, 1994.

[68] S. Kurita, M. Tanaka, and F. Lévy, "Optical spectra near the band edge of zrs 3 and zrse 3," *Physical Review B*, vol. 48, no. 3, p. 1356, 1993.

[69] K. Ueno, "Introduction to the growth of bulk single crystals of two-dimensional transition-metal dichalcogenides," *Journal of the Physical Society of Japan*, vol. 84, no. 12, p. 121015, 2015.

[70] H. Jin, D. Cheng, J. Li, X. Cao, B. Li, X. Wang, X. Liu, and X. Zhao, "Facile synthesis of zirconium trisulfide and hafnium trisulfide nanobelts: Growth mechanism and raman spectroscopy," *Solid State Sciences*, vol. 13, no. 5, pp. 1166–1171, 2011.

[71] S. Tongay, J. Suh, C. Ataca, W. Fan, A. Luce, J. S. Kang, J. Liu, C. Ko, R. Raghunathanan, J. Zhou, *et al.*, "Defects activated photoluminescence in two-dimensional semiconductors: interplay between bound, charged, and free excitons," *Scientific reports*, vol. 3, 2013.

[72] T. Wieting, A. Grisel, F. Levy, and P. Schmid, "Quasi-one-dimensional conductors i," in *Lecture Notes in Physics*, vol. 95, p. 354, Springer-Verlag Berlin, 1979.

[73] J. Harbec, C. Deville Cavellin, and S. Jandl, "Raman spectra and crystal symmetry of zrs3," *physica status solidi (b)*, vol. 96, no. 2, pp. K117–K120, 1979.

[74] R. Loudon, "The raman effect in crystals," *Advances in Physics*, vol. 13, no. 52, pp. 423–482, 1964.

[75] P. Gard, C. Sourisseau, and O. Gorochov, "Effect of metal substitution in zrs3 and tis3 compounds. electronic, raman, and resonance raman study of zr1- xtixs3 ternary phases, 0< x< 1," *physica status solidi (b)*, vol. 144, no. 2, pp. 885–901, 1987.

[76] S. Gwet, Y. Mathey, and C. Sourisseau, "The infrared, raman, resonance raman spectra, and the valence force field of the hfs3 layer-type compound," *physica status solidi (b)*, vol. 123, no. 2, pp. 503–517, 1984.

[77] J. Heyd, G. E. Scuseria, and M. Ernzerhof, "Hybrid functionals based on a screened coulomb potential," *The Journal of Chemical Physics*, vol. 118, no. 18, pp. 8207–8215, 2003.

[78] Y. Jin, X. Li, and J. Yang, "Single layer of mx 3 (m= ti, zr; x= s, se, te): a new platform for nano-electronics and optics," *Physical Chemistry Chemical Physics*, vol. 17, no. 28, pp. 18665–18669, 2015.

[79] L. Fang, X. Zhao, Y.-H. Chiu, D. Ko, K. M. Reddy, T. R. Lemberger, N. P. Padture, F. Yang, and E. Johnston-Halperin, "Comprehensive control of optical polarization anisotropy in semiconducting nanowires," *Applied Physics Letters*, vol. 99, no. 14, p. 141101, 2011.

[80] J. G. Rivas, O. L. Muskens, M. T. Borgström, S. L. Diedenhofen, and E. P. Bakkers, "Optical anisotropy of semiconductor nanowires," in *One-Dimensional Nanostructures*, pp. 127–145, Springer, 2008.

[81] P. Gard, F. Cruege, C. Sourisseau, and O. Gorochov, "Single-crystal micro-raman studies of zrs_3, tis_3 and several $zr_{1-x}ti_xs_3$ compounds ($0< x<0.33$)," *Journal of Raman spectroscopy*, vol. 17, no. 3, pp. 283–288, 1986.